



UNIVERSITÀ
DEGLI STUDI
DI PADOVA

UNIVERSITÀ DEGLI STUDI DI PADOVA

Dipartimento di Ingegneria Industriale DII

Corso di Laurea Magistrale in Ingegneria Aerospaziale

**Dimensionamento del sistema di
controllo d'assetto del PocketQube
RedPill**

Relatore

Lorenzo Olivieri

Studente con matricola

Alessia Dorigatti 2061926

Anno Accademico 2023/2024

Ringraziamenti

In primo luogo, vorrei esprimere la mia sincera gratitudine al mio relatore, il Prof. Lorenzo Olivieri, per il suo continuo supporto e la sua guida esperta durante la scrittura di questa tesi. La sua pazienza, il suo incoraggiamento e i suoi preziosi consigli hanno reso possibile il completamento di questo lavoro, e per questo gli sono profondamente grata.

Ringrazio tutte le persone del progetto J2050 per avermi dato l'opportunità di lavorare con loro su un progetto così stimolante e ricco di sfide. La loro collaborazione e il loro sostegno sono stati fondamentali per il mio sviluppo professionale e personale.

Un ringraziamento speciale va alla mia famiglia, che mi ha sempre sostenuta in ogni fase del mio percorso di studi. Il loro amore incondizionato, il loro incoraggiamento e la loro fiducia in me mi hanno dato la forza di reagire ad ogni difficoltà e di raggiungere questo importante traguardo. Non sarei qui oggi senza di loro.

Un grazie di cuore alla famiglia Luise, che mi ha accolta come una di loro. La loro generosità e affetto mi hanno offerto una seconda casa e un sostegno inestimabile.

Un ringraziamento speciale va anche al mio fidanzato Gio, che mi è sempre stato vicino, anche nei momenti più difficili. Il suo sostegno e il suo amore mi hanno accompagnata e sostenuta fino alla fine di questo percorso.

Un grazie particolare alle mie amiche del liceo, con cui ho condiviso tanti momenti importanti della mia vita. Il loro costante supporto e la nostra duratura amicizia sono per me fonte di grande gioia e forza. Spero che il nostro legame continui a crescere e che la nostra amicizia rimanga sempre così forte.

Infine, voglio ringraziare tutti i miei amici, sia quelli conosciuti a Padova che quelli incontrati durante il mio Erasmus. La loro amicizia e il loro sostegno rendono la mia vita migliore e più ricca. Ogni momento condiviso con loro è stato fonte di felicità e crescita personale.

Sommario

La tesi esplora il controllo d'assetto passivo dei piccoli satelliti di tipo PocketQube attraverso l'uso di magneti permanenti e strisce di isteresi. Lo studio mira a simulare e valutare l'efficacia di questi sistemi di controllo passivo nel ridurre le velocità angolari iniziali e stabilizzare l'orientamento del satellite in orbita.

La tesi inizia introducendo il progetto J2050 e fornendo una panoramica sugli standard e le caratteristiche dei NanoSatelliti, con un focus particolare sui PocketQube. Vengono delineati gli obiettivi della tesi e la sua struttura.

Il quadro teorico tratta la parametrizzazione dell'assetto, utilizzando matrici di rotazione, angoli di Eulero e quaternioni. Si descrivono i vari sistemi di riferimento utilizzati nello studio. Inoltre, si esplora la dinamica dell'assetto ed i disturbi che influenzano i satelliti in orbita. I risultati mostrano come il sistema si stabilizza nel tempo, con un'attenzione particolare alle velocità angolari residue e alle variazioni degli angoli di Eulero.

Le conclusioni sottolineano l'efficacia del controllo d'assetto passivo nei PocketQube, evidenziando miglioramenti rispetto a missioni precedenti e proponendo potenziali aree di miglioramento per il futuro.

Si conclude che i sistemi di controllo passivo con magneti permanenti e strisce di isteresi offrono una soluzione affidabile per la stabilizzazione dell'assetto dei piccoli satelliti.

Abstract

This thesis explores the passive attitude control of small PocketQube-type satellites through the use of permanent magnets and hysteresis strips. The study aims to simulate and evaluate the effectiveness of these passive control systems in reducing initial angular rates and stabilizing the orientation of the satellite in orbit.

The thesis begins by introducing the J2050 project and providing an overview of NanoSatellite standards and characteristics, with a special focus on PocketQubes. The objectives of the thesis and its structure are outlined.

The theoretical framework deals with attitude parameterization, using rotation matrices, Euler angles and quaternions. The various reference systems used in the study are described. In addition, attitude dynamics and disturbances affecting orbiting satellites are explored. The results show how the system stabilizes over time, with a focus on residual angular velocities and changes in Euler angles.

Conclusions emphasize the effectiveness of passive attitude control in PocketQubes, highlighting improvements over previous missions and proposing potential areas for future improvement.

It is concluded that passive control systems with permanent magnets and hysteresis strips offer a reliable solution for attitude stabilization of small satellites.

Contents

1	Introduction	1
1.1	The J2050 project	1
1.2	NanoSatellites standards and overview	2
1.3	Thesis Objectives and structure	3
2	Background and Theoretical Framework	4
2.1	Attitude parametrization	4
2.1.1	Direction Cosine Matrix DCM	5
2.1.2	Euler Angles	5
2.1.3	Quaternions	6
2.2	Reference Frames	7
2.2.1	Body Frame	8
2.2.2	Orbital Frame	8
2.2.3	Earth Centered Inertial Frame	8
2.3	Attitude Dynamics	10
2.4	Attitude Kinematics	11
2.5	Passive Magnetic Stabilization	12
2.5.1	Permanent Magnets	12
2.5.2	Hysteresis Damping	14
2.5.3	Simulink® Simulation	15
3	Overview of the PocketQube	16
3.1	RedPill System Overview	16
3.1.1	Mass Budget	16
3.1.2	Dimensions and moments of Inertia	17
3.1.3	Orbit Determination	18
3.2	Passive Attitude and Orientation Control System Overview	19
3.2.1	Permanent Magnet	19

3.2.2	Hysteresis Strips	21
4	Torque Modeling in Attitude Control	23
4.1	Attitude Propagation	23
4.2	Gravity Gradient Torque	25
4.2.1	Gravity Gradient Torque Modeling	26
4.3	Aerodynamic Drag	27
4.3.1	Aerodynamic Drag Torque Modeling	28
4.4	Solar Radiation Pressure Torque	31
4.5	Magnetic Torque	33
4.5.1	Earth's Magnetic Field	33
4.5.2	Magnetic Torque	37
4.5.3	Hysteresis Damping	39
5	Simulator Verification	45
5.1	Attitude Propagation Verification	45
5.2	Gravity Gradient Verification	46
5.3	Aerodynamic Drag Verification	48
5.4	Earth's Magnetic Field Verification	49
5.5	Permanent Magnet Torque	52
5.6	Hysteresis Damping	53
5.7	Monte Carlo simulation	55
6	Simulation Results and Analysis	59
6.1	Orbit 1 Results	60
6.2	Orbit 2 Results	62
6.3	Summary and Comparative Analysis of ADCS Results	64
7	Conclusions	66
7.1	Limitations and Future Work	67
	Bibliography	68

List of Figures

1.1	PocketQube RedPill	2
2.1	Rotation sequence 321 between two reference frames	6
2.2	Orbital and Body Reference Frames [4]	9
2.3	ECI Coordinate System	9
2.4	Example of Hysteresis Loop [9]	14
3.1	Mass Budget [1]	17
3.2	Orbit and Orbital elements [10]	18
3.3	Exploded with labels [1]	19
4.1	Attitude Propagation	23
4.2	Euler’s Equations subsystem	24
4.3	Quaternion kinematics Subsystem	24
4.4	Gravity Gradient Torque concept [5]	25
4.5	Coordinate System for calculation of Gravity Gradient Torque [5]	26
4.6	Gravity Gradient Torque Modeling	27
4.7	Aerodynamic Drag Torque Overview	28
4.8	Relative velocity in Body coordinates determination	29
4.9	Absorption and Reflection of Incident Radiation [17]	32
4.10	Earth’s magnetic field and magnetic equator [20]	34
4.11	Magnetic field variation with altitude [17]	35
4.12	Simulink implementation of Magnetic Field	36
4.13	Permanent Magnet Torque in Simulink	39
4.14	$B = \frac{2}{\pi} B_s \tan^{-1} [k(H + H_c)]$ [23]	40
4.15	$B = \frac{2}{\pi} B_s \tan^{-1} [k(H - H_c)]$ [23]	41
4.16	Hysteresis Loop [23]	41
4.17	Hysteresis Torque Model	43
5.1	Angular velocities	46

5.2	Euler Angles	46
5.3	20deg/s initial conditions	46
5.4	Gravity Gradient Implementation in MATLAB	47
5.5	Gravity Gradient Torque in both implementations	47
5.6	Aerodynamic Drag Torque	48
5.7	Angle between $\hat{\mathbf{N}}$ and $\hat{\mathbf{V}}$	49
5.8	Comparison between the x Components	50
5.9	Comparison between the y Components	50
5.10	Comparison between the z Components	51
5.11	Errors Earth's Magnetic Field	51
5.12	Permanent Magnet Torque Verification	52
5.13	Hysteresis Cycle for y_{BODY} axis	53
5.14	Hysteresis Cycle for z_{BODY} axis	53
5.15	B_s limit	54
5.16	SNAP hysteresis loop [24]	54
5.17	Mean ω_x angular rate	56
5.18	Mean ω_y angular rate	56
5.19	Mean angular rates	57
5.20	Mean Angle	58
6.1	Body Reference Frame and Euler Angles	60
6.2	Angular Rates in Body Reference Frame Orbit 1	61
6.3	Euler Angles Orbit 1	61
6.4	Permanent Magnet/Earth's Magnetic Field Angle Orbit 1	62
6.5	Angular Rates in Body Reference Frame Orbit 2	62
6.6	Euler Angles in Body Reference Frame Orbit 2	63
6.7	Zoom of Euler Angles	63
6.8	Permanent Magnet/Earth's Magnetic Field Angle Orbit 2	64

List of Tables

3.1	RedPill's Dimensions, Surface Area and Moments of Inertia	17
3.2	Orbit choice	19
3.3	Permanent magnet characteristics	20
3.4	Hysteresis Strips characteristics	21
4.1	Gaussian Coefficients 13 th generation release	37
5.1	Angular Rates Confidence Intervals	57
5.2	Angle Confidence Intervals	58

List of Abbreviations

ADCS	Attitude Determination and Control System
AOCS	Attitude Orientation and Control System
COTS	Commercial Off the Shelf
DCM	Direction Cosine Matrix
IAGA	International Association of Geomagnetism and Aeronomy
IGRF	International Geomagnetic Reference Field
LVLH	Local Vertical Local Horizon
SRP	Solar Radiation Pressure Torque

List of Symbols

Greek Symbols

α	Greenwich sidereal time
μ	Earth's gravitational constant
μ_0	Magnetic permeability of free space
∇	Gradient
ω	Angular rate
ϕ	"Roll" Euler Angle about the x axis
ϕ_m	East longitude of the magnetic dipole
ψ	"Yaw" Euler Angle about the z axis
ρ	Atmospheric density
τ	First point of Aries
θ	"Pitch" Euler Angle about the y axis
θ_m	Coelevation of the magnetic dipole

Roman Symbols

A	area
B	Magnetic field density
C_d	Drag coefficient
c	Speed of light
e	Eccentricity of the orbit
F	Force
h	Altitude of the orbit
h	Angular momentum
H	Magnetic field intensity
i	Inclination of the orbit
I	Inertia matrix
m	Mass
N	Normal to the surface
P	Mean momentum flux
q	Quaternion
R	Rotation Matrix
R_i	Position from center of mass in Aerodynamic Drag
r_i	Distance from center of mass in Aerodynamic Drag
T	Torque
u	Unit vector
V	Velocity
x, y, z	Cartesian components

Subscripts

0	Initial value
1,2,3	Cartesian components
aero	Aerodynamic
B	Body Reference Frame
d	Drag
e	Solar
ext	External component
G	Greenwich
gg	Gravity Gradient
hyst	Hysteresis
i	Infinitesimal component
I	Inertial
mag	Magnetic
O	Orbital Reference Frame
orbit	Orbit component
rel	Relative
SRP	Solar Radiation Pressure
total	Total
x,y,z	Cartesian components

Superscripts

B	Body Reference Frame
I	Inertial Reference Frame
O	Orbital Reference Frame
T	Transposed

Chapter 1

Introduction

This chapter introduces the J2050 mission and its scientific goals. It then explores PocketQubes, a miniaturized satellite technology, ideal for such missions. The chapter also briefly discusses PocketQubes' technical specifications and challenges. Finally, it outlines the goals and structure of this thesis.

1.1 The J2050 project

The J2050 mission, recently selected to participate in the European Space Agency's Fly Your Satellite! program, aims to provide a hands-on experience for the students participating. This initiative, led by the University of Padova, involves the design, development, and launch of a 2P PocketQube satellite [1].

The mission has three primary technological and scientific goals described by the following payloads. Firstly, it aims to explore the feasibility of non-mechanical space telescope covers through the CRYSTALS payload, which employs an innovative electrochemical process to create an anti-light shielding mechanism without moving parts, therefore eliminating additional risks in a satellite's operational life. Secondly, the CLOUD payload will collect in-situ measurements of sub-millimeter debris in Low Earth Orbit (LEO), contributing valuable data to the understanding of space debris environment. Lastly, the CLEAR payload seeks to assess satellite tracking and attitude determination methods by observing LEDs from the ground and utilizing on-board photodiodes for cross-validation. Additionally, the mission aspires to validate a PocketQube bus design for future missions, providing a tested and qualified platform for other universities or institutions at a low cost. By integrating these ambitious objectives, the J2050 mission not only advances space technology and research but also offers students a unique, hands-on educational experience, fostering the next generation of space professionals.

1.2 NanoSatellites standards and overview

Small spacecrafts have been demonstrated to be more effective in terms of science and technology development and to be less expensive than large ones, leading to their increased use in space fields. The spacecrafts that are going to be considered in this thesis are PocketQubes.

PocketQubes, a class of picosatellites introduced by Prof. Bob Twiggs in 2009, they are composed of cubic units measuring 5 x 5 x 5 cm and weighing up to 250 grams per unit, the units are called singularly "P". The PocketQube standard, formalized in 2018 [2], ensures compatibility across different systems and missions by focusing on mechanical dimensions and interface requirements. They are designed to be deployed using systems

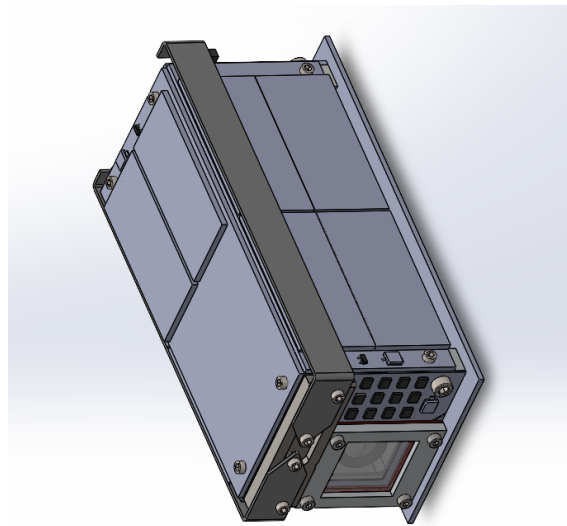


Figure 1.1: PocketQube RedPill

like the AlbaPOD [3], which utilize a baseplate and guide rails for deployment, due to an external addition they couldn't be launched anymore from CubeSat platforms. Their size cause them to be vulnerable to collision with small space debris, which can compromise their structural integrity and operational lifespan. Their low Earth orbit (LEO) placement, where the density of debris is higher, exacerbates this issue. Lifetime of a PocketQube must be also considered and is a critical topic to ensure compliance with the guidelines. Additionally, their limited onboard propulsion and attitude control systems complicate orbit determination and maintenance, often relying on passive stabilization methods that can affect their long-term efficacy. Furthermore, the restricted surface area for solar panels limits their power budget, impacting the satellite's ability to conduct extended missions. These constraints necessitate the development of advanced materials and miniaturized components to enhance the performance and durability of PocketQubes.

Despite these challenges, PocketQubes remain a cost-effective platform for technology demonstration, scientific research, and educational purposes, significantly contributing to space exploration and innovation.

1.3 Thesis Objectives and structure

The main goal of this thesis is to develop an efficient and reliable simulator for the Attitude Orientation and Control System (AOCS) of the J2050 mission, aspiring to replicate real-life conditions of the space environment. The AOCS is a crucial subsystem for any satellite, it maintains the desired orientation of the satellite (such as nadir pointing), resist to external torques and determines the spacecraft's attitude.

For the J2050 mission, Commercial Off-The-Shelf (COTS) components were selected for a predominantly passive AOCS. This system consists of a permanent magnet to maintain attitude and hysteresis strips to perform magnetic damping of the initial angular rate.

The main goals of this thesis are to:

- Create a simulation of the behavior of the satellite in orbit with the MATLAB Simulink tool.
- Analyze the results and refine the design of the AOCS subsystem.

The contents of this thesis can be summarized as it follows:

- Chapter 2: Provides the necessary background, including reference frames, spacecraft kinematics, passive attitude control, and details on the Simulink simulation.
- Chapter 3: Details the architecture of the AOCS in terms of size and type of components used.
- Chapter 4: Defines and describes the simulation of both environmental torques and attitude control torques.
- Chapter 5: Verifies the accuracy and reliability of the simulation.
- Chapter 6: Presents and analyzes the results of the simulation.
- Chapter 7: Summarizes conclusions, and potential improvements.

Chapter 2

Background and Theoretical Framework

In this chapter, a theoretical framework is provided to facilitate a proper understanding of this thesis. The motion of a spacecraft can be divided in two ways: translational motion, described by orbital mechanics, and rotational motion, which pertains to the spacecraft's orientation in space. This thesis will focus on the latter. We will investigate on the attitude parametrizations, define the coordinate frames, and outline the spacecraft's dynamics and kinematics.

2.1 Attitude parametrization

In this section, we delve into the methods used to describe the orientation of a spacecraft, commonly referred to as attitude parametrization. Understanding how to effectively represent and manipulate the attitude is crucial for the design and control of spacecraft systems. We will explore three primary methods: the Direction Cosine Matrix (DCM), Euler Angles, and Quaternions.

Each of these approaches offers unique advantages and limitations, which will be discussed in detail to provide a comprehensive understanding of their applications in the context of the J2050 mission.

This foundational knowledge is essential for developing the Attitude Control System for the spacecraft .

In this section, all of the theoretical principles and formulas can be referenced to these books [4][5].

2.1.1 Direction Cosine Matrix DCM

A possible description of the attitude of a satellite utilizes the rotation matrices. A vector can be expressed in an infinity of reference systems; in this work, the subscript of the vector will indicate the reference system in which it is expressed. Let's represent two different reference frames $A = \{\hat{x}_A, \hat{y}_A, \hat{z}_A\}$ and $B = \{\hat{x}_B, \hat{y}_B, \hat{z}_B\}$ both defined by their unit vectors and sharing the same origin.

A matrix \mathbf{R}_{AB} can always be defined, such as:

$$\mathbf{u}_B = \mathbf{R}_{AB}\mathbf{u}_A \quad (2.1)$$

Where \mathbf{u}_A and \mathbf{u}_B are vectors expressed in the A and B frames, respectively. Therefore, \mathbf{R}_{AB} represents the rotation needed to convert from A to B, thus it can be used to represent the relative orientation (or attitude) of frame **B** with respect to frame **A**.

This matrix is constructed by projecting the unit vectors of frame A onto frame B and placing these projections as the columns of the matrix. Each entry in the matrix is a scalar product between two unit vectors, containing the cosines of the angles between them, hence the name Direction Cosine Matrix. The matrix is represented as:

$$A = \begin{bmatrix} \hat{x}_B \cdot \hat{x}_A & \hat{x}_B \cdot \hat{y}_A & \hat{x}_B \cdot \hat{z}_A \\ \hat{y}_B \cdot \hat{x}_A & \hat{y}_B \cdot \hat{y}_A & \hat{y}_B \cdot \hat{z}_A \\ \hat{z}_B \cdot \hat{x}_A & \hat{z}_B \cdot \hat{y}_A & \hat{z}_B \cdot \hat{z}_A \end{bmatrix} \quad (2.2)$$

The inverse of the matrix is also equal to the transposed, by definition of the properties of orthonormal matrices, so $\mathbf{R}_{BA} = \mathbf{R}_{AB}^{-1} = \mathbf{R}_{AB}^T$. Another important property is that a series of n rotations characterized by the rotation matrices $\mathbf{R}_1, \mathbf{R}_2, \mathbf{R}_3, \dots, \mathbf{R}_n$, is a single rotation, represented by the DCM:

$$\mathbf{R}_{1n} = \mathbf{R}_1\mathbf{R}_2\mathbf{R}_3\dots\mathbf{R}_n \quad (2.3)$$

Although the matrix is described by nine parameters, Euler's rotation theorem requires only three. This could make the use of computational memory less efficient. Nonetheless, the DCM proves to be useful because vector rotations using this representation are simply a matter of matrix multiplication by the DCM.

2.1.2 Euler Angles

Since any attitude in space can be described by three sequential rotations, we will use Eq.(2.3) to describe the attitude of a spacecraft relative to a reference frame. The most

common parameters used are Euler angles, which will also be used in this thesis. ϕ can be defined as the rotation about the X body axis, θ as the rotation about the Y body axis and ψ as the rotation about the Z body axis. Although there are many possible rotation sequences, the most common one is the 3-2-1 sequence, as shown in Fig.2.1: yaw (z-axis), pitch (y-axis), and roll (x-axis). It defines the following DCM matrix (where $c(\cdot)$ and $s(\cdot)$ are abbreviations for $\cos(\theta)$ and $\sin(\theta)$, respectively, to facilitate reading the matrix):

$$\mathbf{R}_{321} = \begin{bmatrix} c_\theta c_\psi & c_\theta s_\psi & -s_\theta \\ -c_\phi s_\psi + s_\phi s_\theta c_\psi & c_\phi c_\psi + s_\phi s_\theta s_\psi & s_\phi c_\theta \\ s_\phi s_\psi + c_\phi s_\theta c_\psi & -s_\phi c_\psi + c_\phi s_\theta s_\psi & c_\phi c_\theta \end{bmatrix} \quad (2.4)$$

However, the use of Euler angles has a significant weakness, known as Gimbal Lock. This occurs when the pitch angle θ is $\pm 90^\circ$, causing two angles to be associated with the same rotation and preventing a unique association (the pitch rotation corresponds to the roll one). The singularity in the matrix implies that, for this sequence to be "correct", it must steer clear of $\pm 90^\circ$ values for the pitch angle. However, this requirement is not acceptable for constructing a reliable and efficient simulator. In the following chapter, we'll explore a possible alternative to this parameterization.

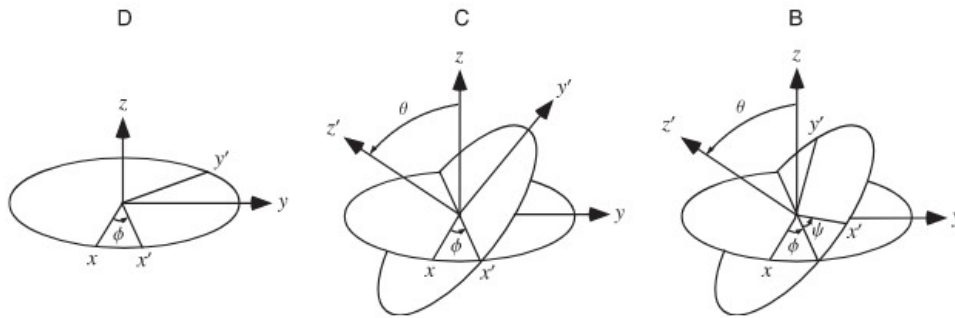


Figure 2.1: Rotation sequence 321 between two reference frames

2.1.3 Quaternions

Quaternions serve as algebraic parameters employed to describe spacecraft attitude, they are useful because they avoid the problem of the gimbal lock that presents itself when describing the attitude using the Euler Angles. Comprising four parameters, they identify the direction of the instantaneous rotation axis and the entity of such rotation.

Represented as a 4x1 matrix with vector and scalar components the quaternion is such as:

$$\mathbf{q} = \begin{bmatrix} q_0 \\ \vec{q} \end{bmatrix} = \begin{bmatrix} q_0 \\ q_1 \\ q_2 \\ q_3 \end{bmatrix} \quad (2.5)$$

with the condition of unitary norm imposed:

$$q_0^2 + \vec{q} \cdot \vec{q} = 1 \quad (2.6)$$

The quaternions don't have a unique definition, literature may interchangeably position the scalar element as q_4 and position it in the last place of the matrix. The parameters are not independent because they have to satisfy the constraint $\|q\| = 1$.

Quaternions uniquely express rotational displacement and can parameterize any rotation. If (\mathbf{t}, α) denotes the rotation transforming frame A into B, the corresponding quaternion is:

$$\mathbf{q} = \begin{bmatrix} \mathbf{t} \sin(\frac{\alpha}{2}) \\ \cos(\frac{\alpha}{2}) \end{bmatrix} \quad (2.7)$$

So it is possible to define the rotation matrix in terms of quaternions:

$$\mathbf{R} = \begin{bmatrix} 1 - 2(q_2^2 + q_3^2) & 2(q_1q_2 - q_0q_3) & 2(q_1q_3 + q_0q_2) \\ 2(q_1q_2 + q_0q_3) & 1 - 2(q_1^2 + q_3^2) & 2(q_2q_3 - q_0q_1) \\ 2(q_1q_3 - q_0q_2) & 2(q_2q_3 + q_0q_1) & 1 - 2(q_1^2 + q_2^2) \end{bmatrix} \quad (2.8)$$

This matrix underscores the advantages of quaternions over the attitude matrix; with only four parameters and one constraint against nine parameters and six constraints imposed by orthogonality, they bypass trigonometric laws and nullify gimbal lock risks. Serving as algebraic instruments, quaternions uniquely define attitude and reveal themselves more useful.

2.2 Reference Frames

In this section, the three primary reference frames utilized throughout this thesis will be outlined. Understanding these frames is crucial for discerning the context of attitude transformations. They are defined using unit vectors, as only vector orientation is pertinent. Some frames may remain inertial, while others experience external acceleration or angular rates relative to the inertial frame, resulting in apparent accelerations for particles or

bodies within them.

The reference frames presented feature an origin and two orthonormal directions, the third chosen in order to complete the triad, forming a right-handed orthonormal triad.

All reference frames discussed in this chapter are referenced in [4].

2.2.1 Body Frame

The Body Frame, denoted as \mathbf{B} in Fig. 2.2, moves along with the spacecraft and delineates its attitude relative to another frame.

Its origin is taken in the center of mass of the spacecraft. The orientation of its axes aligns with the principal axis of inertia of the PocketQube, given that we will consider the z axis the one that points towards the Earth.

This facilitates the definition of Euler Angles rotations as angles about the body axes, they will be such as follows: ϕ about the \mathbf{X}_B axis, θ about the \mathbf{Y}_B axis, and ψ about the \mathbf{Z}_B axis.

This frame plays a crucial role in Attitude and Control, as aligning the spacecraft's orientation with another frame often involves commanding specific angular adjustments relative to the body frame.

2.2.2 Orbital Frame

The Orbital Frame, denoted as \mathbf{R} in Fig. 2.2, is also called Local Vertical Local Horizon (LVLH) and is a frame that moves with the orbital position of the spacecraft. It will be denoted as "O" throughout the attitude description.

Its origin is taken in the center of mass of the spacecraft. The orientation of its axes is defined in accordance with the objective of maintaining a Nadir-pointing attitude (towards the center of the Earth) for the PocketQube spacecraft in this thesis. Consequently, the z-axis aligns with a unit vector directed towards the Earth's center from the spacecraft's center of mass. The x-axis is oriented along the direction of the orbit, pointing in the positive velocity direction. Lastly, the y-axis follows the conventions of a right-handed triad.

2.2.3 Earth Centered Inertial Frame

The Earth Centered Inertial (ECI) Frame, shown in Fig.2.3, has its origin at the center of the Earth. The z axis coincides with the Earth's rotation axis, the x axis extends from the center of the Earth to the vernal equinox Υ (also known as First Point of Aries), and the y axis completes the right-handed triad.

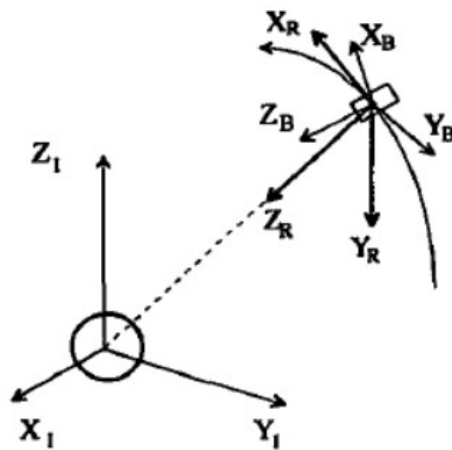


Figure 2.2: Orbital and Body Reference Frames [4]

Although this system is termed inertial, it is not truly so because the Earth rotates around the Sun. However, for the purposes of attitude control in Earth orbit, this acceleration can be neglected.

The vernal equinox, which marks the beginning of spring in the Northern Hemisphere, shifts gradually over time due to the precession of the Earth's axis. This precession causes the equinox to move westward along the ecliptic plane, completing a full cycle approximately every 26,000 years, or 1 degree every 72 years. This phenomenon is known as the precession of the equinoxes. As of now, the vernal equinox point, also known as the First Point of Aries, is located in the constellation of Pisces. For our purposes we can consider it like a fixed point.

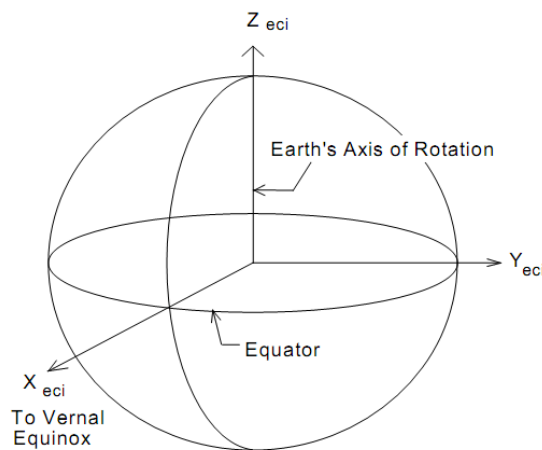


Figure 2.3: ECI Coordinate System

2.3 Attitude Dynamics

This chapter describes the equation of motion for the rotational dynamics of a spacecraft. Dynamics refer to the motion of an object subjected to external torques. Newton's second law on rotational dynamics states that when a body is subjected to an external torque acting about its center of mass, it is equal to the rate of change of its angular momentum.

Identifying as h the angular momentum:

$$\dot{h}_I^{(I)} = T_{\text{ext}}^{(I)} \quad (2.9)$$

The subscript I shows that the law is expressed in an inertial frame, and the derivative of the angular momentum is taken with respect to this frame. The term \mathbf{T}_{ext} comprehends both environmental and control torques. We refer to this dynamic equation as Euler's equations. Euler's equations can also be projected in the body frame, but the rotation of the body frame itself must be considered, as the frame rotates with the body. Thus, the equation Eq.2.9 can be written as:

$$\dot{h}_I^{(B)} = \dot{h}_B^{(B)} + \omega_{BI}^{(B)} \times h^{(B)} = T_{\text{ext}}^{(B)} \quad (2.10)$$

Here, $\omega_{BI}^{(B)}$ is the angular velocity of the body frame relative to the inertial frame, expressed in body coordinates, $\dot{h}_B^{(B)}$ is the derivative of the angular momentum in the body frame. Given that the PocketQube in consideration is rather small and lacks flexible parts, structural analysis is not justified, allowing us to consider the inertia term I_B as fixed in time and in the body frame. Thus, the expression of the angular momentum can be written as $h^{(B)} = [I_B] \omega_{BI}^{(B)}$, This leads to the matrix form of Euler's equation:

$$[I_B] \dot{\omega}_{BI}^{(B)} + \omega_{BI}^{(B)} \times [I_B] \omega_{BI}^{(B)} = T_{\text{ext}}^{(B)} \quad (2.11)$$

Assuming that the body frame is a principal inertial frame (an assumption justified by the minimal values in the mixed product columns/rows in I_B), and denoting $\mathbf{X}_B, \mathbf{Y}_B, \mathbf{Z}_B$ as the principal axes, and performing the vector product, we obtain three scalar equations (we omit the subscripts for simplicity of the formulation):

$$\begin{aligned} I_x \dot{\omega}_x + \omega_y \omega_z (I_z - I_y) &= T_x \\ I_y \dot{\omega}_y + \omega_x \omega_z (I_x - I_z) &= T_y \\ I_z \dot{\omega}_z + \omega_x \omega_y (I_y - I_x) &= T_z \end{aligned} \quad (2.12)$$

These equations, being non-linear, do not have closed-form solutions but can be solved under certain simplifying conditions.

2.4 Attitude Kinematics

The spacecraft's attitude is determined by deriving the kinematics equation. These equations express the spacecraft's angular velocity in the body frame relative to a non-inertial orbital frame, denoted as ω_{BO} .

Integrating the Euler's equations yields the angular velocity of the body frame relative to the inertial frame, denoted as ω_{BI} . The relationship between these two velocities is explained by the formula:

$$\omega_{BI}^{(B)} = \omega_{BO}^{(B)} + \omega_{OI}^{(B)} \quad (2.13)$$

where $\omega_{OI}^{(B)}$ is the angular velocity of the orbital frame relative to the inertial frame expressed in body coordinates.

Since the inertial frame is supposed to be the ECI frame, we define the angular velocity $\omega_{OI}^{(O)}$ of the orbital frame relative to the inertial frame in orbital coordinates as $\omega_{OI}^{(O)} = [0, -\omega_{orbit}, 0]^T$ where ω_{orbit} is the orbital angular velocity. Given that the orbit of the J2050 mission is circular, it can be calculated as $\omega_{orbit} = \sqrt{\frac{\mu}{r^3}}$, where μ is the Earth's gravitational constant and r the radius from the Earth's center to the spacecraft.

The angular velocity vector can be transformed in body coordinates by premultiplying a transformation matrix such as \mathbf{R}_{OB} , yielding:

$$\omega_{OI}^{(B)} = \mathbf{R}_{OB}\omega_{OI}^{(O)} \quad (2.14)$$

\mathbf{R}_{OB} is obtained from kinematics equations as follows:

$$\mathbf{R}_{OB} = (q_0^2 - \vec{q} \cdot \vec{q})\mathbf{I} + 2\vec{q}\vec{q}^T - 2q_0\mathbf{A} \quad (2.15)$$

where \vec{q} represents the vectorial part of the quaternion defined as $\vec{q} = (q_1, q_2, q_3)^T$, and \mathbf{A} is defined as:

$$\mathbf{A} = \begin{bmatrix} 0 & -q_3 & q_2 \\ q_3 & 0 & -q_1 \\ -q_2 & q_1 & 0 \end{bmatrix}$$

To avoid singularities and time-consuming parametrizations like Direction Cosine Matrices (DCM), we express the kinematics equations in quaternion form:

$$\dot{\mathbf{q}} = \frac{1}{2}[\mathbf{Q}]\mathbf{q} = \frac{1}{2} \begin{bmatrix} 0 & -\omega_x & -\omega_y & -\omega_z \\ \omega_x & 0 & \omega_z & -\omega_y \\ \omega_y & -\omega_z & 0 & \omega_x \\ \omega_z & \omega_y & -\omega_x & 0 \end{bmatrix} \begin{bmatrix} q_0 \\ q_1 \\ q_2 \\ q_3 \end{bmatrix} \quad (2.16)$$

Given the initial condition \mathbf{q}_0 , we can integrate the quaternion to determine the attitude variation over time. It's important to highlight that integrating quaternions is simpler and avoids encountering singularities compared to integrating Euler's equations and Direction Cosine Matrices (DCM).

2.5 Passive Magnetic Stabilization

This section explores the techniques used for magnetic stabilization in satellite systems, with a particular focus on the J2050 spacecraft. Magnetic stabilization is essential for keeping a satellite stable and correctly oriented while in orbit.

We will discuss the use of a permanent magnet in the J2050, which interacts with the Earth's magnetic field to create stabilizing forces. Additionally, we will look at hysteresis strips, which help dissipate rotational energy and further stabilize the satellite. These strips work by interacting with the magnetic field to reduce unwanted movements.

This overview will highlight the key methods used in the J2050's stabilization system, emphasizing their role in maintaining satellite orientation and ensuring the success of its mission.

2.5.1 Permanent Magnets

Attitude control using permanent magnets is a utilized technique in satellite systems, particularly for smaller satellites such as nanosatellites. This method leverages the Earth's magnetic field to stabilize and orient the satellite. A permanent magnet, installed onboard the spacecraft, creates a magnetic dipole that interacts with the Earth's geomagnetic field. This interaction generates a torque that aligns the satellite's magnetic axis with the geomagnetic field vector, providing passive stabilization.

The use of permanent magnets for attitude control presents several notable challenges. First, the method is inherently limited in precision. The interaction with the geomagnetic

field only provides a rough alignment, making it unsuitable for missions that require high-precision orientation. The passive nature of the system means that fine adjustments cannot be made once the satellite is in orbit.

Moreover, it will not be possible to control the rotation of the satellite around the dipole axis, making this attitude control technique not ideal for satellites that require continuous precise pointing.

Another challenge is the variability of the Earth's magnetic field, which changes with location and time. These fluctuations can lead to variations in the stabilizing torque, causing periodic oscillations in the satellite's orientation. This variability can complicate the design and operation of the attitude control system, requiring careful planning and simulation to predict and mitigate its effects. Additionally the intensity of the Earth Magnetic field weakens with the increase of the distance from its center, varying as the inverse of r^3 , where r being the distance of the spacecraft from the center of the Earth. Therefore this technique is not suitable for spacecrafts in high orbits.

Additionally, the process of designing an effective permanent magnet system involves complex considerations. The placement and properties of the permanent magnet must be optimized to maximize its stabilizing effect while minimizing potential interference with other satellite components. This requires detailed numerical simulations and testing to ensure the system performs as intended under various orbital conditions.

The first Russian nanosatellite, TNS-0, that has an AOCS that is comparable to the one analyzed in this thesis, provides a practical example of the use and challenges of permanent magnet-based attitude control. TNS-0's attitude control system included a permanent magnet that interacted with the Earth's magnetic field to provide stabilization. The design team faced several challenges, including optimizing the magnet's placement and ensuring it did not interfere with other satellite components. Numerical simulations were used to predict the satellite's behavior, taking into account the interactions between the magnetic components and the satellite's inertial properties.

Despite the challenges, TNS-0's mission demonstrated the effectiveness of permanent magnet-based attitude control for low-precision stabilization tasks. The system successfully reduced chaotic rotations and maintained a stable orientation, suitable for the satellite's operational requirements. This example highlights the potential of permanent magnet-based systems for certain mission profiles, while also underscoring the need for careful design and planning to address the inherent limitations and challenges of this approach, [6][7].

2.5.2 Hysteresis Damping

Hysteresis damping is an effective method for stabilizing the attitude of satellites and to help to remove an initial tumble rate, by utilizing the magnetic properties of certain materials to dissipate rotational kinetic energy as heat. This passive damping technique is particularly valuable in space applications where simplicity, reliability, and low power consumption are fundamental.

The principle of hysteresis damping relies on the behavior of soft magnetic materials when subjected to a changing magnetic field, such as the one that would be experienced by a spacecraft orbiting around the Earth. These materials have magnetic domains that align with an external magnetic field. When the field is removed, the domains do not return entirely to their original orientation, resulting in residual magnetization. This behavior is depicted by the hysteresis loop, which shows the relationship between magnetic flux density (B) and magnetic field strength (H). The area within the hysteresis loop represents the energy lost per cycle due to internal friction within the material [8]. A generic hysteresis loop is represented in Fig.2.4. The B-H curve for these materials provides insights

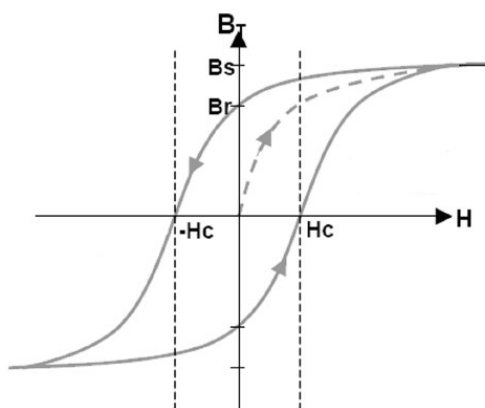


Figure 2.4: Example of Hysteresis Loop [9]

into their energy dissipation capabilities and helps in selecting appropriate materials for hysteresis rods.

In satellite applications, hysteresis damping is implemented using rods or thin strips made of soft magnetic materials with high permeability. These rods are placed within the satellite, often aligned with its spin axis. As the satellite rotates, the Earth's magnetic field induces changes in the magnetic flux within these rods. The continuous realignment of the magnetic domains within the rods generates internal friction, which dissipates rotational energy as heat. This process effectively dampens the satellite's rotational motion, reducing unwanted oscillations and stabilizing its attitude [9].

In practice, hysteresis strips are strategically placed within the satellite to interact opti-

mally with the Earth's magnetic field and to minimize perturbations on the permanent magnet's magnetic field too. This interaction generates a damping torque proportional to the magnetic field component along the satellite's spin axis. The dynamic realignment of the magnetic dipoles within the rods as the satellite moves through its orbit ensures continuous energy dissipation, thereby maintaining the desired attitude stability. This method is particularly useful for small satellites, where the constraints on power, weight, and complexity make passive solutions like hysteresis damping highly desirable [8][9].

Hysteresis damping offers several advantages, including simplicity, reliability, and the absence of moving parts or active control systems. However, its effectiveness can be limited by the specific properties of the hysteresis material and the configuration of the rods. Proper design and material selection are essential to maximize the damping efficiency and ensure the stability of the satellite throughout its mission [8].

In summary, by converting rotational kinetic energy into heat through internal friction, hysteresis rods help maintain the desired attitude of the satellite, ensuring stable operation and reducing the risk of uncontrolled tumbling. This passive damping technique is an integral part of modern satellite attitude control systems, offering a reliable and efficient solution for maintaining stability in space.

2.5.3 Simulink® Simulation

Simulink®, a robust tool integrated within the MATLAB environment, stands as a cornerstone for graphical modeling and simulation tasks, providing an intuitive platform for crafting and analyzing dynamic systems. Throughout the course of this thesis, Simulink® emerged as an indispensable asset in simulating the Passive Attitude Determination and Control System (ADCS).

Utilizing its graphical interface and extensive library of tools, Simulink® facilitated the development of a comprehensive simulation model for the passive ADCS. Leveraging its differential equation solvers, the simulation model accurately captured the time-varying dynamics of the ADCS under varying conditions.

In summary, Simulink® played a pivotal role in the simulation of the passive ADCS presented in this thesis, offering a versatile platform for modeling and analyzing complex dynamic systems.

Chapter 3

Overview of the PocketQube

This chapter provides a comprehensive overview of the physical characteristics of the RedPill PocketQube, including its mass, dimensions, and moments of inertia.

Additionally, the chapter discusses the types of orbits considered in the simulation and details the architecture of the passive magnetic Attitude and Orientation Control System (AOCS). Specific emphasis is placed on the materials used in the construction of the passive control system.

This detailed description aims to establish a foundational understanding of the RedPill PocketQube's physical properties and the principles behind its passive stabilization mechanisms.

3.1 RedPill System Overview

This section will provide a comprehensive overview of the general characteristics of the PocketQube, following the guidelines outlined in [2] as a 2P PocketQube and ensuring compliance with established standards.

It is important to note that the distribution and positioning of masses significantly impact certain spacecraft characteristics. For instance, the moments of inertia are directly affected by how the masses are arranged within the PocketQube. Additionally, the mission's specific goals and objectives play a pivotal role in determining the optimal orbit selection.

These mission parameters can influence various design and operational aspects of the PocketQube, tailoring its functionality to meet the intended mission requirements.

3.1.1 Mass Budget

The mass budget, outlined in [1], indicates a total system mass of 387.6 g. With a 20% margin applied, this amounts to 456.1 g. For simulation purposes, the most up-to-date

mass term of $m = 388 \text{ g}$ and is adopted from the updated CAD model of the PocketQube. Fig.3.1 shows the mass budget for all components, the permanent magnets do not have a major influence on the mass budget as they are minimal due to size constraints.

Component	Mass [g]	Qty.	Total [g]	Margin [%]	Total with margin [g]
TTC					
Deployable antenna	19	1	19	5	20
Transceiver	1	1	1	5	1
TOT			20		21
OBC					
TOT			23	20	28
AOCS					
Permanent magnets	9	3	27	20	32
TOT			27		32
ST&M					
2P structure	19	1	19	5	20
TOT			19		20
EPS					
BMS	10	1	10	5	11
MPPT PCB	9	1	9	20	11
Battery holder	28	1	28	20	34
Solar cells	4	12	48	5	50
Battery	18	4	73	5	77
TOT			168		183
PCB					
Sensor debris (-Y)	25	1	25	5	26
Sensor debris (+Y)	20	1	20	5	21
Bridge (-Z)	9	1	9	5	9
Bridge (+Z)	13	1	13	5	14
TOT			67		70

Figure 3.1: Mass Budget [1]

3.1.2 Dimensions and moments of Inertia

The dimensions of the PocketQube are taken from the most updated version of the CAD, this parameter is very important because it directly affects environmental disturbances such as Aerodynamic Drag and Gravitational Gradient, crucial considerations for worst-case scenario dimensioning.

The table below presents dimensions, surface areas (pertinent for Aerodynamic Drag), and moments of inertia all evaluated under worst-case conditions and implemented in MATLAB initialization code. These values are referenced in the Body Reference Frame as discussed in Section 2.2.1.

	x	y	z
Dimensions [m]	$5.00 \cdot 10^{-2}$	$5.00 \cdot 10^{-2}$	$11.4 \cdot 10^{-2}$
Surface Area [m^2]	$5.70 \cdot 10^{-3}$	$5.70 \cdot 10^{-3}$	$2.50 \cdot 10^{-3}$
Moments of Inertia [kgm^2]	$0.501 \cdot 10^{-3}$	$0.501 \cdot 10^{-3}$	$0.162 \cdot 10^{-3}$

Table 3.1: RedPill's Dimensions, Surface Area and Moments of Inertia

In this simulation, we assume that the center of mass coincides with the geometric center of the PocketQube for simplicity. However, future simulations will incorporate a more detailed representation of its shape to enhance accuracy.

3.1.3 Orbit Determination

Orbit determination considers two cases, each defined by orbital elements including:

- h : Altitude from the Earth's surface.
- e : Eccentricity of the orbit.
- i : Inclination from the Earth's equatorial plane.
- Ω : "RAAN" Right Ascension of the Ascending Node, the angle between the Node Line (point where the orbit crosses the equator) and the Right Ascending Node.
- w : "AOP" Argument of Perigee, the angle between the Node Line and positioning of the perigee.
- θ : "TA" True Anomaly, the start angle between the perigee and the start of the orbit.

These elements are illustrated in Fig. 3.2, and further explanations can be found in [10]. The two orbits chosen are reported in Tab.3.2.

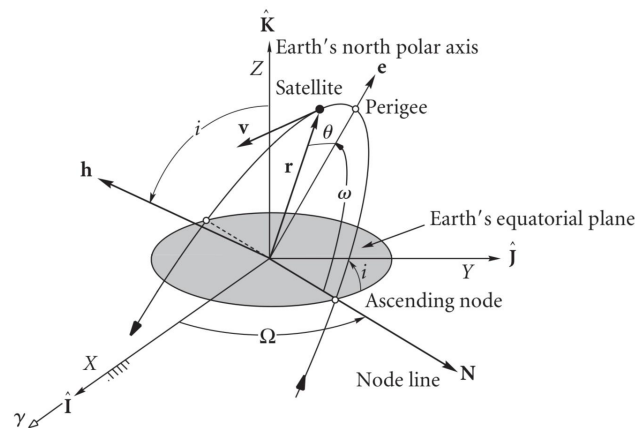


Figure 3.2: Orbit and Orbital elements [10]

Both orbits are circular with an altitude of 450 km. The altitude selection ensures worst-case environmental disturbances [1]: gravitational torque varies with Earth distance, and Aerodynamic Drag Torque varies with atmospheric thickness, greater at lower altitudes. Different inclinations explore how magnetic field direction influences AOCS, crucial for

	h [km]	e	i [deg]	RAAN [deg]	AOP [deg]	TA [deg]
Orbit 1	450	0	45.5	215	0	0
Orbit 2	450	0	98	304.2	0	0

Table 3.2: Orbit choice

magnetic control alignment with field lines.

Lastly, RAAN positions the spacecraft's ground track to pass over Padova, as it is planned to locate a ground station on an university building.

3.2 Passive Attitude and Orientation Control System Overview

This chapter aims to offer a comprehensive overview of the AOCS subsystem, detailing its physical characteristics and orientation. It will also provide a thorough description of the materials used and their expected performance.

For a better visual aid, the exploded image of the PocketQube¹ with all the subsystems is provided below.

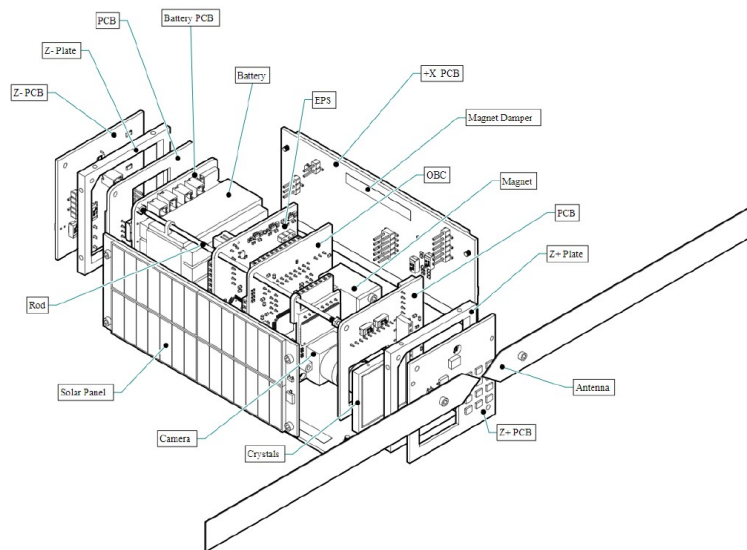


Figure 3.3: Exploded with labels [1]

3.2.1 Permanent Magnet

Permanent magnets are essential components in various technological applications due to their ability to maintain a persistent magnetic field without the need for continuous exter-

¹The image may not reflect the latest arrangement of subsystems due to ongoing changes in the process. However, the overall schematic remains consistent.

nal power.

Among the different types of permanent magnets, neodymium (NdFeB) magnets stand out for their exceptional magnetic properties, making them ideal for high-performance applications such as passive Attitude and Orbit Control Systems (AOCS) for PocketQubes.

Neodymium magnets, often referred to as NdFeB magnets, are composed primarily of neodymium (Nd), iron (Fe), and boron (B), forming the compound $Nd_2Fe_{14}B$. These magnets are part of the rare-Earth magnet family and are renowned for their high magnetic strength and energy product, which is the maximum energy density they can store.

The high remanence (Br) and coercivity (Hc) of neodymium magnets contribute to their superior performance in applications requiring strong and stable magnetic fields, it is important to notice that their high coercivity make them able to maintain their magnetization even with demagnetizing fields applied [11][12].

The N45 grade of neodymium magnets is particularly notable for its high magnetization. The grade indicates specific magnetic properties, with N45 representing a maximum energy product (BHmax). This high energy product translates to a stronger magnetic field and greater holding force, making N45 magnets suitable for compact and efficient designs required in small-scale space applications like PocketQubes [13].

The key characteristics and dimensions of the N45 Neodymium permanent magnet used are summarized in the table below. The permanent magnet in question will be placed with

Characteristic	Value
Total mass [g]	27.6
Total volume [mm^3]	3600
Total dimension [mm]	20 x 20 x 9
Magnetization Grade	N45
Remanence Br [T]	1.32-1.38
Energy Product BHmax [MGOe]	42-45
Temperature Range [$^{\circ}C$]	-138/80

Table 3.3: Permanent magnet characteristics

its dipole axis orientated as the x axis in the Body Reference Frame (see Section 2.2.1), the axis in the direction of the velocity. This orientation has been selected as the optimal configuration for the PocketQube based on extensive simulations and logical reasoning. It has been verified that orienting the magnet in this manner minimizes environmental disturbances and potential torque effects on the satellite.

In the context of a passive AOCS for a PocketQube, neodymium magnets serve as the primary components for maintaining the satellite's orientation relative to the Earth's magnetic field. By strategically placing N45 neodymium magnets within the satellite, it is

possible to achieve passive stabilization. The magnetic dipole created by the magnets interacts with the geomagnetic field, generating a restoring torque that aligns the satellite along a desired orientation [14][15].

The high remanence and coercivity of N45 magnets ensure that the magnetic dipole remains strong and stable over the satellite’s operational life, even in the harsh conditions of space. Additionally, the compact size and high magnetic strength of these magnets allow for efficient use of limited space and mass within the PocketQube, which is critical for meeting the stringent design constraints of small satellites.

3.2.2 Hysteresis Strips

Hysteresis strips play a crucial role in passive Attitude and Orbit Control Systems (AOCS) for small satellites like PocketQubes. These strips, made from materials with high magnetic permeability and low coercivity, such as HyMu 80, are used to provide magnetic damping, which is essential for stabilizing and controlling the satellite’s attitude.

HyMu 80 is a high-permeability nickel-iron alloy specifically engineered for applications requiring superior magnetic performance. This alloy typically consists of approximately 80% nickel and 20% iron, which imparts it with outstanding magnetic properties. The high initial permeability (μ) and low coercivity (H_c) of HyMu 80 make it an excellent choice for hysteresis damping in space applications [16].

The properties of the selected material are listed in the table below. They are composed by two hysteresis strips that will be placed with the magnetic axis in the direction of y_B and z_B with respect to the Body Reference Frame (see Section 2.2.1), in order to dampen the angular rate but also in order to not interfere with the permanent magnet. Where, it is

Characteristic	y axis	z axis
Total dimension [mm]	5.00x38x0.355	5.00x98.4x0.355
Total volume [mm^3]	67.5	175
Coercivity (H_c) [A/m]	1.59	1.59
Remanence Br [T]	0.361	0.361
Saturation Induction (B_s) [T]	0.730	0.730

Table 3.4: Hysteresis Strips characteristics

remembered that:

- Coercivity (H_c): The magnetic field strength needed to demagnetize the strip.
- Remanence (Br): The residual magnetization retained by the strip after removing the external magnetic field.

- Saturation Induction (B_s): The maximum magnetic flux density the strip can achieve under given conditions.

These properties make HyMu 80 hysteresis strips highly effective for damping oscillations and stabilizing the attitude of a PocketQube through magnetic interaction with the Earth's geomagnetic field [11][16].

The damping effect of the HyMu 80 hysteresis strips is crucial for reducing residual oscillations and stabilizing the satellite's attitude over time. By dissipating the rotational kinetic energy as heat, the hysteresis strips ensure that the satellite maintains its desired orientation with minimal power consumption and without the need for active control mechanisms [12].

Chapter 4

Torque Modeling in Attitude Control

This chapter delves into the nature and modeling of both environmental and control torques exerted on the Redpill spacecraft. It details the methods used to model these torques in Simulink.

The explanation of how the verifications of the reliability of the models were conducted will be explained in the next chapter.

4.1 Attitude Propagation

The goal of this section is to explain how the spacecraft's attitude is propagated using Simulink, making easier to understand the subsequent topics. To illustrate this, the attitude propagation model is shown in Fig.4.1.

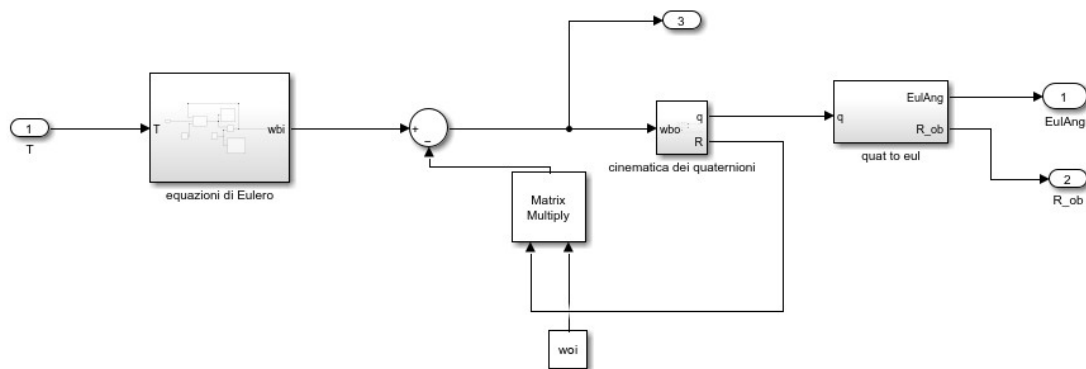


Figure 4.1: Attitude Propagation

As depicted in the image, the input to this model consists of the torques (both environmental and control) expressed in body coordinates. These torques are fed into the first subsystem, which implements Euler's equations, as seen in Eq.2.12. The output of this

subsystem is the satellite's angular rate ω_{BI} . This output is then summed with ω_{OI} , which has been transformed into body coordinates using the transformation matrix. This summation block implements the equation Eq.2.13.

The next subsystem handles the quaternion kinematics, producing the quaternions that are subsequently processed to obtain the Euler angles describing the attitude.

A closer look at the Euler's equations block is provided in Fig.4.2.

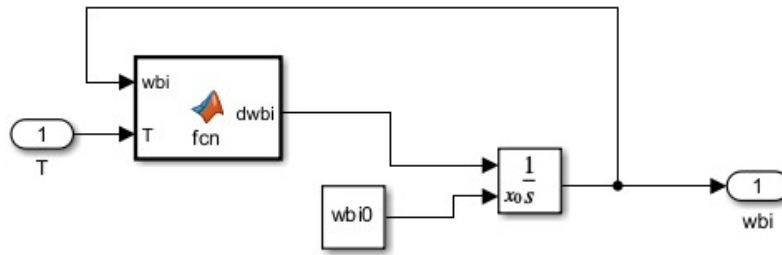


Figure 4.2: Euler's Equations subsystem

The MATLAB function block within this subsystem implements the equations detailed in Eq.2.12. The output $\dot{\omega}_{BI}$ is then integrated with the initial condition given $\omega_{OI}^{(0)} = [0, -\omega_{orbit}, 0]^T$ as already mentioned in section 2.4.

Next, we delve into the quaternion kinematics subsystem, shown in Fig.4.3.

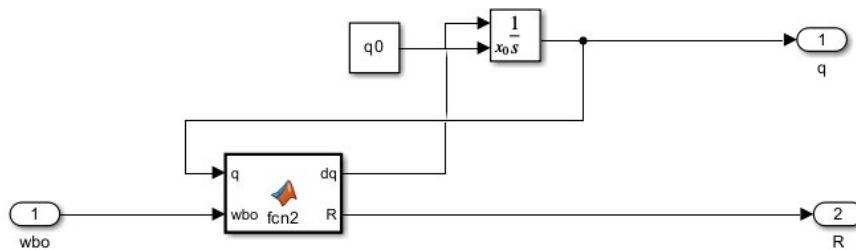


Figure 4.3: Quaternion kinematics Subsystem

In this subsystem, the MATLAB function block implements Eq.2.16 and the rotation matrix **A** also described in the same section.

Finally, the "quat to eul" block converts the quaternions to Euler angles, providing the spacecraft's attitude.

4.2 Gravity Gradient Torque

To describe the Gravity Gradient Torque, we will refer to the theory explained in [17]. The Gravity Gradient torque is exerted on every non-symmetrical object that orbits around the Earth, due to the variation in the Earth's gravitational force on the object. This can be visualized in Fig.4.4, as a scenario where an object's side is closer to the Earth and experience certain gravity force stronger than the side further away. This imbalance creates a torque about some axis of the object, causing a variation of its attitude.

In this section we are going to assume the inertia tensor known in a body frame whose

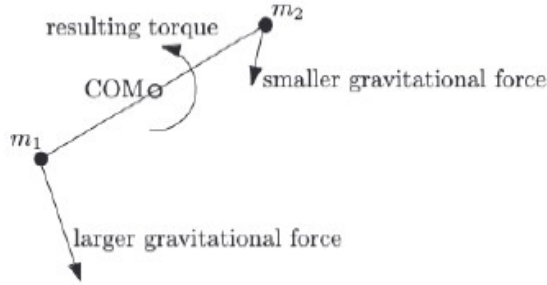


Figure 4.4: Gravity Gradient Torque concept [5]

origin does not coincide with the center of mass, and that the spacecraft is orbiting a spherical Earth.

The gravitational force $d\mathbf{F}_I$ exerted on a spacecraft element dm_i located in a position \mathbf{R}_i from the geometric center, we can write:

$$d\mathbf{F}_I = \frac{-\mu\mathbf{R}_i dm_i}{R_i^3} \quad (4.1)$$

where μ is the Earth's gravitational constant The torque exerted about the spacecraft's geometrical center due to a force $d\mathbf{F}_I$ at a position \mathbf{r}_i can be expressed as:

$$d\mathbf{T}_{gg} = \mathbf{r}_i \times d\mathbf{F}_I = (\rho + \mathbf{r}'_i) \times d\mathbf{F}_I \quad (4.2)$$

Where ρ is measured from the geometric center of mass, \mathbf{r}'_i from the center of mass to the mass element dm_i , as can be seen in Fig.4.5.

The torque can be obtained by integrating the terms in Eq.4.2 and we can obtain:

$$\mathbf{T}_{gg} = \int \mathbf{r}_i \times d\mathbf{F}_I = \int (\rho + \mathbf{r}'_i) \times \frac{-\mu\mathbf{R}_i}{R_i^3} dm_i \quad (4.3)$$

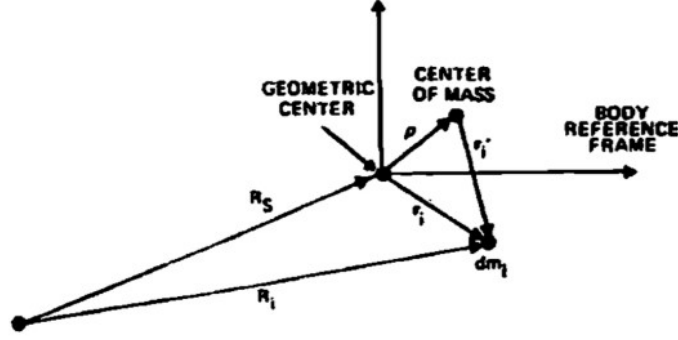


Figure 4.5: Coordinate System for calculation of Gravity Gradient Torque [5]

Assuming $\rho = 0$ in order for the geometric center and the center of mass to coincide (as assumed in J2050 simulations) and defining \mathbf{r}_i and $\hat{\mathbf{R}}_s$ along the body reference axes, the gravity gradient torque can be expressed as:

$$\mathbf{T}_{gg} = \frac{3\mu}{R_s^3} [\hat{\mathbf{R}}_s \times (I \cdot \hat{\mathbf{R}}_s)] \quad (4.4)$$

where I is the moment of inertia tensor.

4.2.1 Gravity Gradient Torque Modeling

This section will explain the modeling of the gravity gradient torque within the Simulink simulation framework. The torque exerted on a spacecraft orbiting the Earth can be expressed as this:

$$\begin{aligned} \mathbf{T}_{ggx} &= +\frac{3\mu}{r_0^3} |I_z - I_y| R_{OB}(2,3) R_{OB}(3,3) \\ \mathbf{T}_{ggy} &= -\frac{3\mu}{r_0^3} |I_z - I_x| R_{OB}(1,3) R_{OB}(3,3) \\ \mathbf{T}_{ggz} &= -\frac{3\mu}{r_0^3} |I_x - I_y| R_{OB}(1,3) R_{OB}(2,3) \end{aligned} \quad (4.5)$$

In this context μ represents the Earth's gravitational constant, the matrix \mathbf{R}_{OB} (as per Eq.2.15) is the transformation matrix from the orbital reference frame to the body reference frame where $R_{OB}(i,j)$ are its components, finally r_0 is the vector from the center of the Earth to the spacecraft.

It's worth noting that considering the standard dimensions of PocketQubes, we will have for a 2U PocketQube such as RedPill: $I_x \approx I_y$, minimal or no gravity gradient torque will be generated around the z axis of the body reference frame. This torque will tend to align the axis of minimum inertia of the Cubesat with the local vertical, the Z_{body} axis.

This observation underscores a restoring torque phenomenon, crucial for maintaining a nadir pointing attitude in nadir-pointing spacecrafts, particularly when the attitude deviation from equilibrium is minimal.

The torque is implemented in the simulation with this scheme of blocks in Fig.4.6.

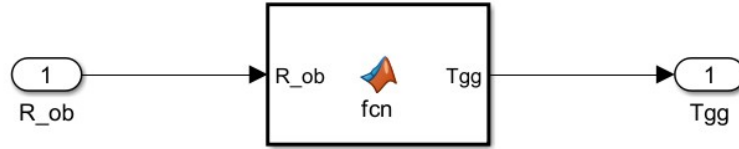


Figure 4.6: Gravity Gradient Torque Modeling

From the image, it is evident that the implementation of this torque is straightforward. Within the Matlab function block the series of equations written in Eq.4.5, in Body reference frame coordinates, are implemented. Parameters such as μ , I and r_0 are imported in the function as fixed parameters from the initialization code on Matlab. The only input needed is the transformation matrix one, that is imported from the attitude propagation block.

This simple implementation provides the Gravity Gradient torque, which is subsequently integrated into the attitude propagation block.

4.3 Aerodynamic Drag

All the theoretical framework regarding the Aerodynamic Torque can be referred to [17]. Aerodynamic drag is an environmental torque that acts on a spacecraft due to the interaction with the residual atmosphere, causing resistance and rotational forces. This torque arises from the interaction between a spacecraft's surface and the upper atmosphere. The force due to the impact of molecules on the surface can be modeled as an elastic impact without reflection, meaning the particles lose all their energy upon impact.

The elemental aerodynamic force, $d\mathbf{F}_{aero}$ acting on a surface element $d\mathbf{A}$ is defined as:

$$d\mathbf{F}_{aero} = -\frac{1}{2}C_d\rho V_{rel}^2 (\hat{\mathbf{N}} \cdot \hat{\mathbf{V}}) \hat{\mathbf{V}}d\mathbf{A} \quad (4.6)$$

Here, $\hat{\mathbf{V}}$ is the unit vector representing the spacecraft's translational velocity, $\hat{\mathbf{N}}$ is the unit normal vector of the surface, ρ is the atmospheric density and C_d is the coefficient of the aerodynamic drag. If detailed aerodynamic informations are not available, it can be

generally considered 2.0 for practical applications. In the context of the J2050 mission this parameter is considered to be equal to 2.2, due to observations of similarities with the FossaSat-1 picosatellite [18].

The torque generated by the Aerodynamic Drag, \mathbf{T}_{aero} , acting on a surface can then be defined as:

$$\mathbf{T}_{aero} = \int r_s \times d\mathbf{F}_{aero} \quad (4.7)$$

where r_s is the vector from the center of mass to the surface of the element dA . The integral is performed only on surfaces where is valid the expression $\hat{\mathbf{N}} \cdot \hat{\mathbf{V}} > 0$.

To analyze the torque distribution, we can divide the PocketQube into simple geometric shapes, such as its six sides. The total torque can then be obtained by summing the individual torques acting on each surface element.

The force, as defined in [17], acting on a normal surface of area A and having normal to the area $\hat{\mathbf{N}}$ is:

$$T_{aero} = -\frac{1}{2}C_d\rho V^2 A (\hat{\mathbf{N}} \cdot \hat{\mathbf{V}}) \hat{\mathbf{V}} \quad (4.8)$$

4.3.1 Aerodynamic Drag Torque Modeling

This subsection explains how the torque produced by Aerodynamic Drag was modeled in the simulation, with all applied formulas referring to the previous section.

A general overview image is provided below, in order to help with visual aid.

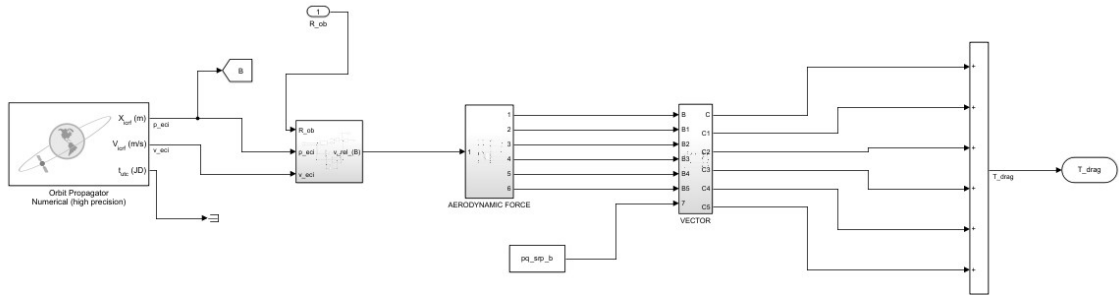


Figure 4.7: Aerodynamic Drag Torque Overview

Some of the modeling concepts and blocks can also be referred to [19].

We will explore the first block, illustrated in the Fig.4.8. Firstly we are going to define the velocity that appears in Eq.4.6. According to [19], this term can be defined as:

$$\mathbf{V}_{relI} = \mathbf{V}_I + \omega_I \times r_I \quad (4.9)$$

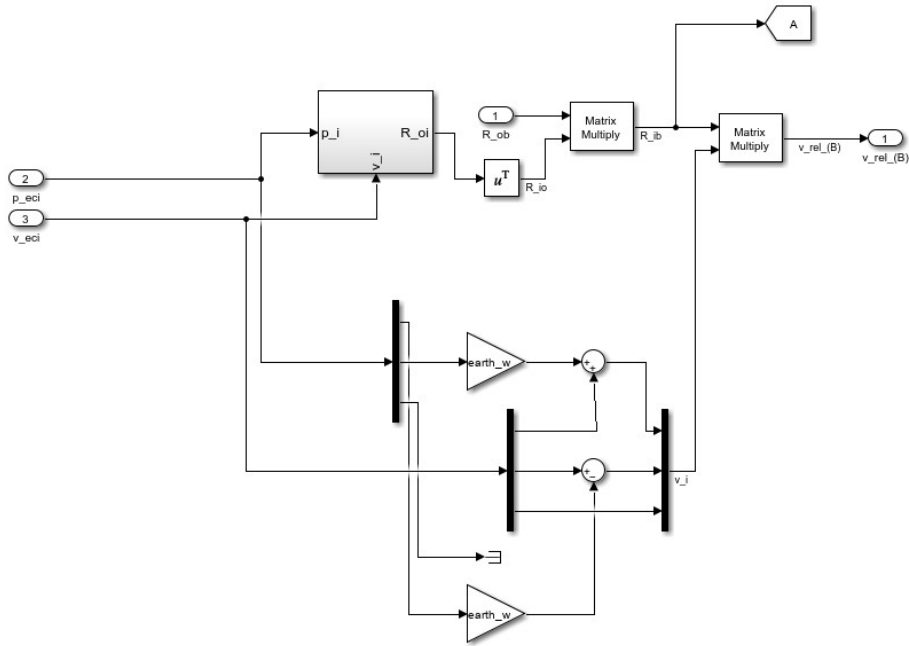


Figure 4.8: Relative velocity in Body coordinates determination

Here, \mathbf{V}_I and r_I are the velocity and position in the ECI frame (see Section 2.2.3), ω is the Earth's rotational rate. The vector that specifies the Earth's rate is $\omega_I = [0, 0, 7.2921e - 05]^T \text{ rad/s}$, then this formula can be written as:

$$V_{rel} = \begin{bmatrix} \dot{x} + \omega y \\ \dot{y} - \omega x \\ \dot{z} \end{bmatrix} \quad (4.10)$$

Since this vector is expressed in the ECI reference frame and the velocity in body reference frame is needed, it must be converted using a combination of rotation matrices. The final rotation matrix can be obtained using the relation

$$R_i^b = R_i^o R_o^b = R_o^i R_o^b \quad (4.11)$$

The theory in [19] is helpful for this transformation. It shows that the rotation from the orbital frame to the inertial frame can be expressed as:

$$\begin{aligned}\mathbf{o}_{3I} &= -\frac{r_I}{\|r_I\|} \\ \mathbf{o}_{2I} &= -\frac{r_I \times V_I}{\|r_I \times V_I\|} \\ \mathbf{o}_{1I} &= \mathbf{o}_{2I} \times \mathbf{o}_{3I}\end{aligned}\tag{4.12}$$

The matrix is given by:

$$\mathbf{A} = [o_{1I}, o_{2I}, o_{3I}]\tag{4.13}$$

To obtain the rotation matrix from inertial to orbital coordinates the relation in Eq.4.11 is used. By multiplying this rotation matrix with the relative velocity, the expression for the relative velocity in body reference frame can be derived \mathbf{v}_{rel}^B .

The ECI position and velocity are propagated through a Simulink Block that serves the purpose¹.

The formula that defines the Aerodynamic Drag Force is implemented in a MATLAB function block and can be alternatively defined, from Eq.4.6 by the formula (in [19]):

$$\mathbf{F}_{aero}^i = -\frac{1}{2}\rho C_D \|\mathbf{V}_{rel}\| \mathbf{V}_{rel} S_i \max(\cos \theta_{aero}^i, 0)\tag{4.14}$$

An important observation is that both conditions $\hat{\mathbf{N}} \cdot \hat{\mathbf{V}} > 0$ and $\max(\cos \theta_{aero}^i, 0)$ signify that these equations exclude the surfaces of the spacecraft that do not directly face the incoming atmospheric flux relative to the spacecraft's orbital velocity. These surfaces are not taken into account because they do not contribute to the generation of Aerodynamic Drag Torque. This selection ensures that only the relevant spacecraft surfaces interacting with the atmospheric flow are considered in calculating the torque.

The following formula defines the cosines of the angles between the normal of the surface and the velocity vector:

$$\cos \theta_{aero}^i = \frac{\mathbf{n}_B^i \cdot \mathbf{v}_{rel}^B}{\|\mathbf{v}_{rel}^B\|}\tag{4.15}$$

Finally the torque can be defined, as in [19], as:

$$\mathbf{T}_{aero}^i = \sum_{i=1}^N \mathbf{r}^i \times \mathbf{F}_{aero}^i\tag{4.16}$$

¹<https://it.mathworks.com/help/aeroblks/orbitpropagator.html>

Where \mathbf{r}^i is the vector from the center of mass to the center of pressure of the plate considered.

As already mentioned in the previous section this torque will be considered for all of the six faces of the PocketQube and summed to obtain the total torque.

Here is a simplified scheme of the process:

1. Through the propagator and the application of Eq.4.10, V_{rel}^i is obtained.
2. The relative velocity is then multiplied by the transformation matrix in Eq.4.11.
3. The cosine angles are implemented as in Eq.4.15.
4. The Aerodynamic Force is implemented through a MATLAB function block as defined in Eq.4.14.
5. All the results of the Aerodynamic Drag Force are then multiplied as Eq.4.16, every one of them with the respective vector.
6. The torques for each of the six faces are then summed to produce the total torque output.

4.4 Solar Radiation Pressure Torque

The Solar Radiation Pressure (SRP) Torque is not implemented in the current simulation, as it is considered negligible compared to other torques. However, for completeness, its theoretical foundations in this section are going to be specified.

The theoretical concepts and formulas in this section can be referred to [17].

The SRP Torque arises when the radiation of the Sun impacts on the spacecraft's surface, generating a force that results into a torque about the center of mass of the spacecraft. This force diminishes inversely with the square of the distance from the Sun, making it essentially altitude independent for Earth-orbiting spacecrafts.

The major factors influencing this torque are:

- The intensity and spectral distribution of the incident radiation
- Geometry of the surface and optical properties
- Orientation of the Sun vector relative to the spacecraft

Regarding the first factor, we can consider the direct solar radiation only, as it is significantly stronger than both Earth albedo and Earth emitted radiation.

The mean momentum flux can be defined as:

$$P = \frac{F_e}{c} \quad (4.17)$$

Here, F_e is the solar constant and c is the speed of light. The solar constant exhibits minor periodic variations due to the Earth's elliptical orbit around the Sun, and its value is also wavelength-dependent.

For many applications it is considered that the force is either absorbed, reflected specularly or reflected diffusely [17], as illustrated in Fig.4.9.

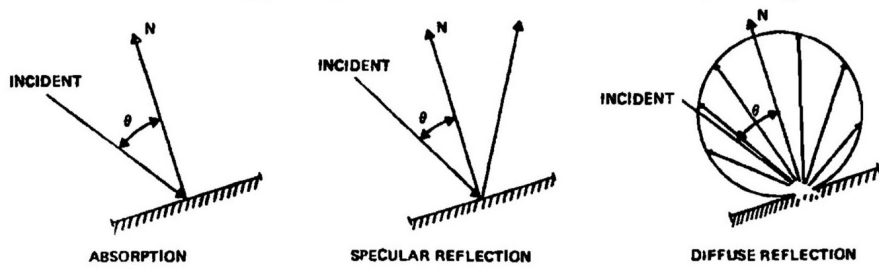


Figure 4.9: Absorption and Reflection of Incident Radiation [17]

The force generated on a plane with surface area A and normal $\hat{\mathbf{N}}$ can be expressed as:

$$\mathbf{F}_{SRP_{total}} = -PA \cos(\theta) \left[(1 - C_s) \hat{\mathbf{S}} + 2 \left(C_s \cos(\theta) + \frac{1}{3} C_d \right) \hat{\mathbf{N}} \right] \quad (4.18)$$

Where, $\hat{\mathbf{N}}$ is the unit vector normal to the surface and $\hat{\mathbf{S}}$ is the unit vector from the spacecraft to the Sun.

In this formula C_a , C_s and C_d are the absorption, specular reflection and diffused reflection coefficients and they have to be $C_a + C_s + C_d = 1$.

The total SRP torque is given by:

$$\mathbf{T}_{SRP_{total}} = \sum_{i=1}^N \mathbf{R} \times \mathbf{F}_{SRP_{total}} \quad (4.19)$$

Here \mathbf{R} is the vector from the center of mass to the center of SRP pressure of the surface area. Similar to aerodynamic drag, the spacecraft is considered as being divided into N -plates, with the total torque being the sum of the torques acting on each plate.

4.5 Magnetic Torque

This section provides a detailed exploration of the modeling of magnetic torques and the simulation of Earth's magnetic field within MATLAB and Simulink.

We will delve into the specifics of modeling both permanent magnet torque and hysteresis damping, outlining the theoretical foundations and methodologies used for their implementation.

By examining these components, this section aims to establish a clear understanding of how the Earth's magnetic field was accurately represented and how magnetic torques were integrated into the simulation framework.

These insights are crucial for the comprehensive analysis and prediction of spacecraft dynamics in varying magnetic environments.

4.5.1 Earth's Magnetic Field

In this subsection we will explore both the spherical harmonic model and the dipole approximation that aims to represent the Earth's magnetic field in the most reliable way possible. All theoretical concepts and considerations can be referred to [17].

The Earth's magnetic field can be approximated as a magnetic dipole, the one that can be produced by a current loop, for example. The dipole characteristics change with time, the strength is decreasing by 0.005% per year, the secular drift implies a possible reversal in several thousand years [17]. The plane perpendicular to the dipole is called geomagnetic equator, where the field is at its weakest. Since the dipole rotates with the Earth, it indicates that it originates within it. A representation of the equator is given in Fig.4.10.

It is also worth of mention the fact that the magnetic field decreases as $\frac{1}{R^3}$, making applications that exploit the Earth's magnetic field become less and less effective with the increasing of the altitude. Fig.4.11 shows the variation of the magnetic field with altitude.

The magnetic field can be expressed as the gradient of a scalar potential V :

$$\mathbf{B} = -\nabla V \quad (4.20)$$

The absence of magnetic monopoles implies:

$$\nabla \cdot \mathbf{B} = 0 \quad (4.21)$$

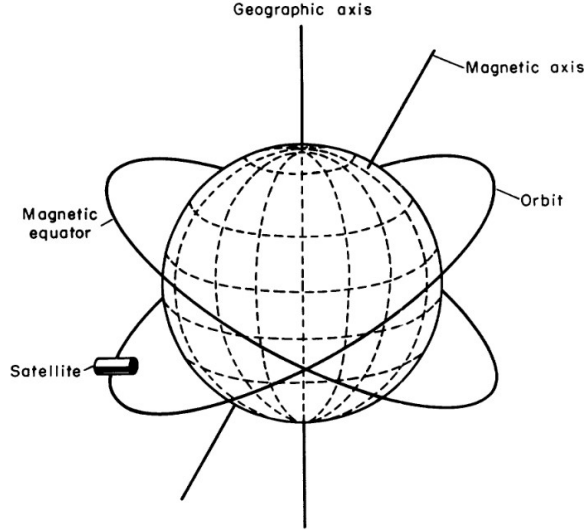


Figure 4.10: Earth's magnetic field and magnetic equator [20]

Substituting Eq.4.20 in Eq.4.21 results in Laplace's equation:

$$\nabla^2 V = 0 \quad (4.22)$$

V can be expressed as a series of spherical harmonics:

$$V(r, \theta, \phi) = a \sum_{n=1}^k \left(\frac{a}{r}\right)^{n+1} \sum_{m=0}^n (g_n^m \cos(m\phi) + h_n^m \sin(m\phi)) P_n^m(\theta) \quad (4.23)$$

Here, a is the equatorial radius of the Earth, g_n^m and h_n^m are Gaussian coefficients, r , θ and ϕ are the geocentric distance, coelevation and East longitude from Greenwich, respectively.

The Gaussian coefficients are defined empirically, a set of these coefficients define a model of the field, the first ones of them are defined secular.

Although this definition of the field is more accurate, it requires significant computing power. Therefore it is more convenient to define the field as a dipole model, expanding these spherical terms in the first degree ($n=1$) and all orders ($m=0,1$).

The Eq.4.23 then becomes:

$$V(r, \theta, \phi) = \frac{a^3}{r^2} [g_1^0 P_1^0(\theta) + (g_1^1 \cos(\phi) + h_1^1 \sin(\phi)) P_1^1(\theta)] \quad (4.24)$$

Skipping the detailed mathematical steps (found in [17]), we use the dominant component of the dipole model to approximate the magnetic field expression as a vector dipole \mathbf{m} .

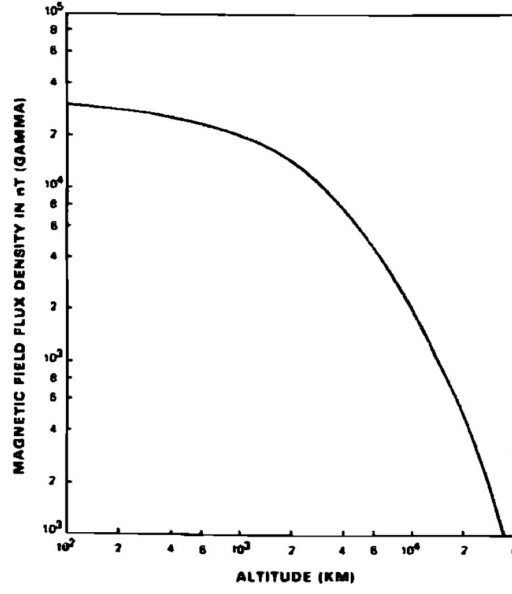


Figure 4.11: Magnetic field variation with altitude [17]

Thus, it can be written as:

$$\mathbf{B}(\mathbf{R}) = \frac{a^3 H_0}{R^3} [3(\hat{\mathbf{m}} \cdot \hat{\mathbf{R}})\hat{\mathbf{R}} - \hat{\mathbf{m}}] \quad (4.25)$$

Here, \mathbf{R} is the position vector at which the field is desired. Since this is a vector equation, \mathbf{B} can be expressed in any convenient frame. The dipole strength is expressed by the formula:

$$a^3 H_0 = a^3 \left[g_1^{02} + g_1^{12} + h_1^{12} \right]^{\frac{1}{2}} \quad (4.26)$$

For our case study it is convenient to express it in the ECI frame (discussed in Section.2.2.3). The dipole can be characterized in terms of:

$$\hat{\mathbf{m}} = \begin{bmatrix} \sin\theta'_m \cos\alpha_m \\ \sin\theta'_m \sin\alpha_m \\ \cos\theta'_m \end{bmatrix} \quad (4.27)$$

Where θ'_m is the coelevation of the dipole and is expressed by:

$$\theta'_m = \arccos \left(\frac{g_1^0}{H_0} \right) \quad (4.28)$$

Consequently, α_m is defined by:

$$\alpha_m = \alpha_{G0} + \frac{d\alpha_G}{dt}t + \phi'_m \quad (4.29)$$

Here, α_{G0} is equal to the Greenwich sidereal time at reference time and date, $\frac{d\alpha_G}{dt}$ is the average rotation of the Earth, t is the time since reference. Finally, ϕ'_m is the East longitude of the dipole:

$$\phi'_m = \arctan\left(\frac{h_1^1}{g_1^1}\right) \quad (4.30)$$

Lastly the magnetic field in ECI is:

$$\begin{aligned} B_x &= \frac{a^3 H_0}{R^3} \left[3(\hat{\mathbf{m}} \cdot \hat{\mathbf{R}})R_x - \sin\theta'_m \cos\alpha_m \right] \\ B_y &= \frac{a^3 H_0}{R^3} \left[3(\hat{\mathbf{m}} \cdot \hat{\mathbf{R}})R_y - \sin\theta'_m \sin\alpha_m \right] \\ B_z &= \frac{a^3 H_0}{R^3} \left[3(\hat{\mathbf{m}} \cdot \hat{\mathbf{R}})R_z - \cos\theta'_m \right] \end{aligned} \quad (4.31)$$

Here, R_x , R_y and R_z are the expressions of the position in ECI coordinates.

Earth magnetic Field Modeling

This subsection will delve into the modelation of the magnetic field in Simulink, specifying some of the values chosen for the specific simulation in the context of the J2050 mission.

The Fig.4.12 represents visually how the Earth's Magnetic field is modeled within Simulink, it will also be explained how the Gaussian coefficients were chosen.

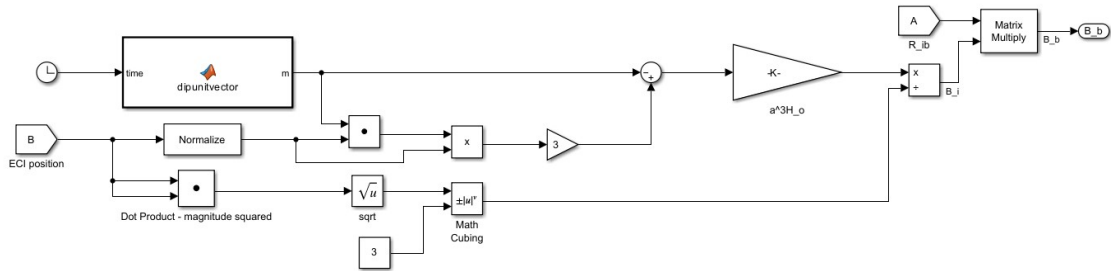


Figure 4.12: Simulink implementation of Magnetic Field

The "From" block labeled "B" implements the position of the Spacecraft in ECI, as already shown in Section 4.3.2, the blocks that follow implement the algebraic operations of the Eq.4.31. The MATLAB function block labeled "dipoleunitvector" implements the definition of the dipole vector given by Eq.4.27. Here, the Gaussian components were calculated with reference to the latest IGRF 13th Schmidt semi-normalised spherical harmonic coefficients release by IAGA [21], the first degree and first order used ones are shown in the table below, taken directly from the spreadsheet provided.

The values for the year 2020 were chosen as they are the most recent and updated, and

cos/sin	Degree	Order	IGRF
g/h	n	m	2020
g	1	0	-29404,8
g	1	1	-1450,9
h	1	1	4652,5

Table 4.1: Gaussian Coefficients 13th generation release

they are close to the mission start date (1 Jan 2025), making them a reasonable approximation.²

With these values it was possible to determine the constants in the Eq.4.31. The first one was a^3H_0 , the expression of H_0 given in Eq.4.26 is 29805.69, then multiplied with the value of the radius of the Earth.

Subsequently $\theta'_m = 170.59^\circ$, $\phi'_m = 107.32^\circ$, as given in Eq.4.28 and Eq.4.30, respectively.

The expression α_0 in Eq.4.29 was calculated for a date of 0th UTC of the 1st of January of 2025, it was found directly on MATLAB combining two algorithms provided by the book [10], it resulted equal to $\alpha_0 = 100.9^\circ$.

The final expression of the Earth's Magnetic dipole unit vector at the beginning of the mission is:

$$\hat{\mathbf{m}} = \begin{bmatrix} -0.0487 \\ 0.156 \\ -0.986 \end{bmatrix} \quad (4.32)$$

The MATLAB function has as input a "Clock" block to implement the time of the simulation in Eq.4.29.

Finally, the magnetic field in Inertial Reference Frame coordinates is multiplied by the "From" block labeled "A" that gives the rotation matrix from Inertial Frame to the Body frame, as explained in the previous section.

4.5.2 Magnetic Torque

A magnetic dipole, when immersed in a magnetic field, experiences a torque that aligns it with the local field, much like a compass needle. Magnetic dipoles can also be generated by the transient currents of electronic devices, these parasitics currents can generate torques that will destabilize the spacecraft. In other cases anyway, magnetic control can

²These considerations were given by empirical observations of the rate of change of these values. As an example, g_1^0 was equal to -30654 in 1935, it is now equal to -29404,8, so in five years the difference would be minimal and not significant.

be used to control the attitude of a spacecraft.

As discussed in Section 2.5.1 permanent magnets align with the Earth's magnetic field to prevent random tumble [22].

The torque exerted by a dipole \mathbf{m} immersed in a magnetic field \mathbf{B} is given by:

$$\mathbf{T}_{mag} = \mathbf{m} \times \mathbf{B} \quad (4.33)$$

Eq.4.33 shows that the relationship involves a cross product, which means that this type of control torque can't produce a torque about the dipole axis. Consequently, this will lead to the spacecraft to spin freely about this axis in an uncontrolled way. This is the main limitation of magnetic control. However, techniques such as employing hysteresis strips can mitigate this issue. Hysteresis strips provide passive damping by dissipating energy through magnetic hysteresis, thereby reducing the spacecraft's angular velocity and helping to achieve a more stable orientation.

In this case study the dipole produced by a permanent magnet can be defined by this equation:

$$m = \frac{BV}{\mu_0} \quad (4.34)$$

Here, B is the magnetic flux density of the magnet, V the volume and μ_0 the magnetic permeability of free space. This equation provides a straightforward way to calculate the magnetic dipole moment based on the physical properties of the magnet used in the spacecraft.

It's important to notice that careful design is necessary in order to balance the magnetic dipole moment and ensure effective stabilization without introducing unwanted rotations. Additionally, the interaction with Earth's magnetic field must be thoroughly analyzed to optimize the placement and strength of the magnets.

Magnetic Torque Modeling

The Magnetic Torque due to the permanent magnet is relatively easy to model, as illustrated in Fig.4.13.

As can be seen from the figure the permanent magnet dipole that is in input is implemented in the initializing code in MATLAB, so it will be easier to modify. The input B_b is the Earth's magnetic field in Body coordinates implements in the previous section.

The output will be the torque in Body coordinates.

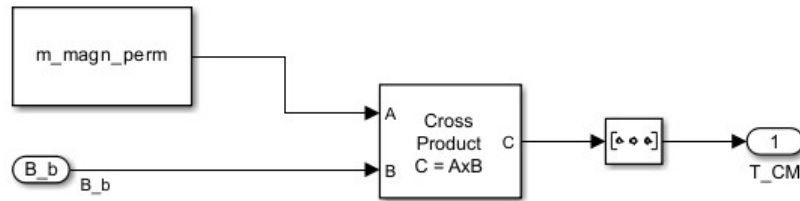


Figure 4.13: Permanent Magnet Torque in Simulink

4.5.3 Hysteresis Damping

Angular rate damping is a challenge in passive control systems because space offers no friction, allowing a spacecraft to roll uncontrollably about an axis. Hysteresis damping provides a solution to this problem.

While active systems use reaction wheels or magnetic coils for angular rate damping, passive systems can achieve this through hysteresis strips made of soft ferromagnetic material. As already discussed in Section 2.3.2 the angular rate damping using hysteresis strips means that when immersed in a field such as one of the Earth, these devices will dissipate kinetic energy in the form of heat, as a sort of friction.

Fig.2.4 illustrates a typical magnetic hysteresis curve, where H_c represents coercivity, B_r denotes remanence, and B_s signifies the saturation magnetic flux density. As the magnetic field (H) cycles while the satellite rotates through it, the material undergoes magnetization and demagnetization along the hysteresis curve. The energy lost as heat during each cycle is represented by the area within the hysteresis loop.

Magnetic coercivity is the intensity of the external magnetic field applied in the opposite direction of the material's magnetization that is required to reduce the magnetization to zero after the material has been driven to saturation. Remanence, on the other hand, is the residual magnetic flux density that remains in the material after the external magnetic field is removed. It indicates how well a material can retain its magnetization; high remanence means significant magnetization is retained, while low remanence suggests rapid loss of magnetization. Saturation Induction (B_s) is the maximum magnetic flux density the strip can achieve under given conditions.

The lag, or "hysteresis," in the material's response to an externally applied magnetic field is due to both coercivity and remanence. This lag results in energy being lost as heat within the material. This phenomenon can be understood as the magnetic dipoles experiencing

”friction” as their orientation changes.

This loss is due to the non-frictionless flipping of magnetic domains within the material. For effective magnetization and demagnetization by the Earth’s magnetic field, a material must have sufficiently low coercivity (H_c). Additionally, high permeability enhances the effectiveness of hysteresis.

The behaviour of hysteresis strips rely critically on the definition of the curve ”B/H” of the specific material, where B is the magnetic flux density and H is the magnetic intensity. The model used can be referenced to [23], where functions and algorithms provide a close approximation to empirical data.

We will skip the detailed mathematical considerations from the referenced article, but it is essential to note that these derivations lead to defining functions that describe the behavior of both sides of the hysteresis loop faithfully.

The equation that describes the left boundary of the loop is:

$$B = \frac{2}{\pi} B_s \tan^{-1} [k(H + H_c)] \quad (4.35)$$

where k is:

$$k = \frac{1}{H_c} \tan \left(\frac{\pi B_r}{2 B_s} \right) \quad (4.36)$$

This is illustrated in figure Fig.4.14.

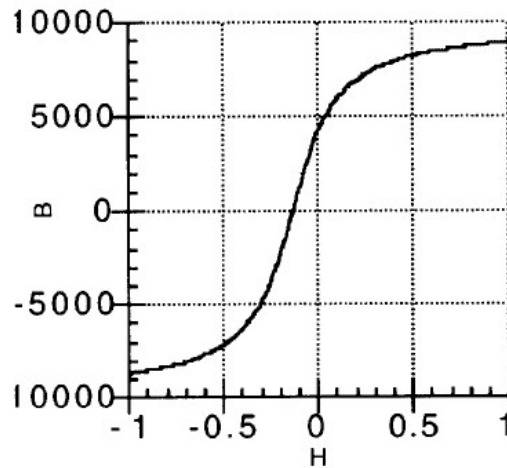


Figure 4.14: $B = \frac{2}{\pi} B_s \tan^{-1} [k(H + H_c)]$ [23]

The right boundary of the loop is represented by:

$$B = \frac{2}{\pi} B_s \tan^{-1} [k(H - H_c)] \quad (4.37)$$

This formula is obtained by shifting the original curve to the right by the same amount H_c , as shown in Fig.4.15.

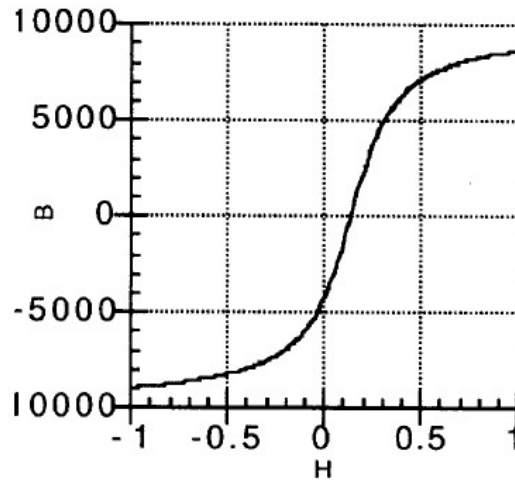


Figure 4.15: $B = \frac{2}{\pi} B_s \tan^{-1} [k(H - H_c)]$ [23]

Finally we can superimpose the two curves and obtain the resemblance of the typical magnetic hysteresis loop shown in Fig.4.16.

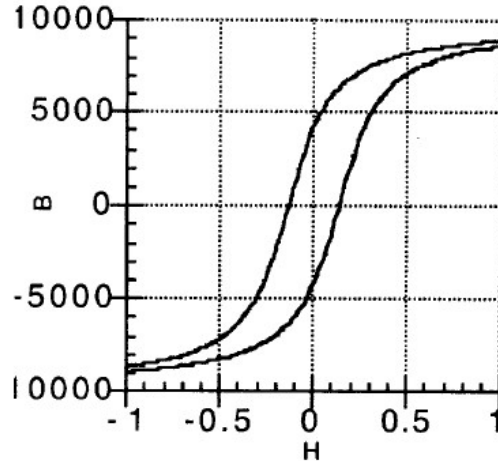


Figure 4.16: Hysteresis Loop [23]

In [23] an algorithm is provided to determine $\frac{dB}{dt}$, the rate of the magnetic density, which will be used to implement the hysteresis behaviour in Simulink. Other parameters introduced earlier are useful for a more precise definition of the hysteresis loop. The steps of the algorithm are given below.

Given B the "magnetic flux density", H the "magnetizing field", $\frac{dH}{dt}$, with k^3 , q_0 and p

³The k constant can be determined by Eq:4.36, q_0 and p must be determined through a trial and error process. In this case of study they have been determined equal to the ones in [22] simulation, because of the

predetermined constants, where q and q_0 are boundary slope multipliers and k a predetermined constant.

The algorithm is given by:

1. Compute H_L , given by inverting the formula

$$B = \frac{2}{\pi} \tan^{-1} [k(H_L + H_C)]$$

corresponding to the left boundary curve.

2. Find B' , the boundary curve slope corresponding to the value of B . The formula needed is:

$$B' = \frac{2}{\pi} k B_s \cos^2 \left(\frac{\pi B}{2 B_s} \right)$$

3. Find the value $f = \frac{H - H_L}{2H_c}$
4. Check if f is negative, then we will measure f from the right boundary

$$\frac{dH}{dt} < 0 \implies f = 1 - f$$

5. Find $q = q_0 + (1 - q_0) f^p$

6. Determine $\frac{dB}{dH} = qB'$

7. Finally

$$\frac{dB}{dt} = \frac{dB}{dH} \frac{dH}{dt}$$

These steps implement the "friction" generated by the hysteresis behaviour of the strips and are implemented through a MATLAB function block in Simulink, the result $\frac{dB}{dt}$ is then integrated through a block in Simulink as will be shown after.

Hysteresis Damping Modeling

The "magnetizing field" (H) is the component of the external magnetic field aligned with the axis of the magnetic dipole. This field induces a "magnetic flux density" (B) within the material, resulting in a magnetic moment that is also parallel to the axis. The interaction between this magnetic moment and the external field generates a torque, which can be

similarity of the ferromagnetic characteristics of the materials used. It resulted in: $k = 0.6$, $q_0 = 0.0855$ and $p = 4.75$

utilized to reduce the spin of satellites.
 The expression of torque produced is:

$$\mathbf{T}_{hyst} = \hat{\mathbf{m}} \times \mathbf{B} \quad (4.38)$$

The magnetic moment is given by:

$$\hat{\mathbf{m}} = \frac{\mathbf{B}_{hyst} V_{hyst}}{\mu_0} \quad (4.39)$$

The modeling of the overall torque is illustrated in Fig.4.17. The subsystem operates as

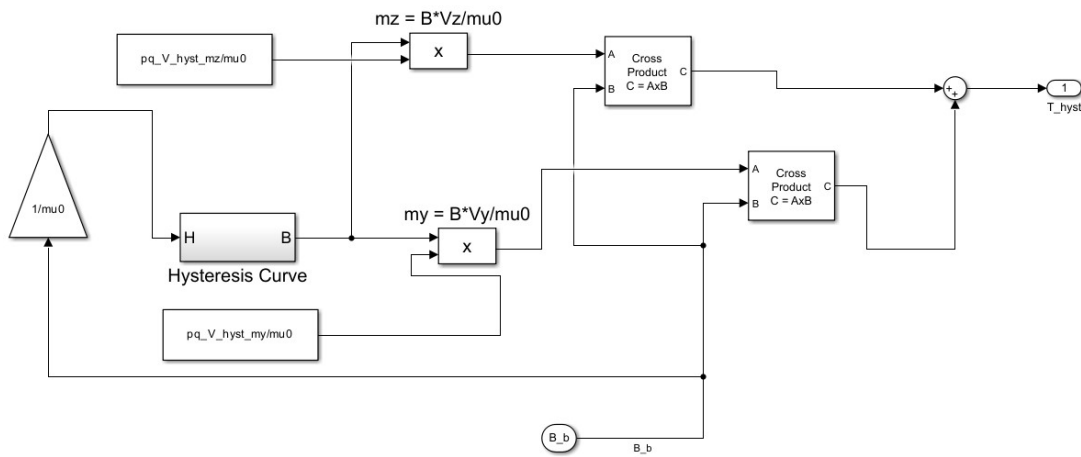


Figure 4.17: Hysteresis Torque Model

follows:

1. The Earth's magnetic field density \mathbf{B}_{Earth} is input in body coordinates from the block that models the Earth's magnetic field.
2. The Earth's magnetic field intensity is calculated through multiplying by the gain $\frac{1}{\mu_0}$.
3. The magnetic field density is determined using the block "Hysteresis Curve" that models all the concepts explained before.
4. The magnetic moment is then found by multiplying as Eq.4.39.
5. Then the magnetic torque is obtained by the cross product with the Earth's magnetic field as described in Eq.4.38.

By utilizing the interaction between the induced magnetic moment and the external magnetic field, this method generates torque, providing an alternative to active control systems.

Chapter 5

Simulator Verification

This chapter details the comprehensive series of verifications undertaken to ensure the robustness and reliability of the program. The purpose of these verifications is to systematically evaluate the program's performance, identify and resolve any potential issues, and confirm that it meets the specified requirements and expectations.

Each input torque will be individually tested and verified to ensure it meets the expected values. Whenever possible, these results will be compared against an existing model to further confirm their accuracy.

By documenting these processes, the aim is to provide a thorough understanding of how the program's quality was assessed and to demonstrate the commitment to delivering a reliable and effective solution. This chapter serves as a testament to the meticulous efforts invested in verifying the program's integrity and performance.

5.1 Attitude Propagation Verification

In this section the propagation of the spacecraft's attitude will be verified to ensure it meets the expected values.

Initially, a straightforward validation will be conducted by placing the spacecraft in nadir configuration with an initial rotational rate of zero when no torques or rotations are applied. The objective is to confirm that the spacecraft maintains an attitude of zero degrees.

These verifications will be carried out using Orbit Type 1 (refer to Section 3.1.3). The initial conditions are set as $q_0 = [1; 0; 0; 0]$ and $w_{oi} = [0; -\sqrt{\mu/r0^3}; 0] \frac{rad}{s}$, where $-\sqrt{\mu/r0^3}$ is the rotational velocity of the circular orbit. This setup ensures that the simulation begins with the spacecraft in a nadir initial configuration.

The resulting angular velocities of the spacecraft in the Body Reference Frame and the corresponding Euler angles are illustrated below in Fig.5.1 and Fig.5.2.

Another validation will involve imparting an initial tumble rate to the spacecraft and

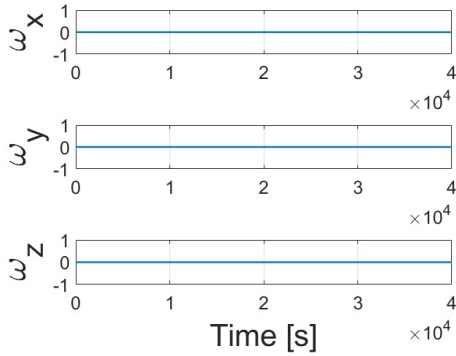


Figure 5.1: Angular velocities

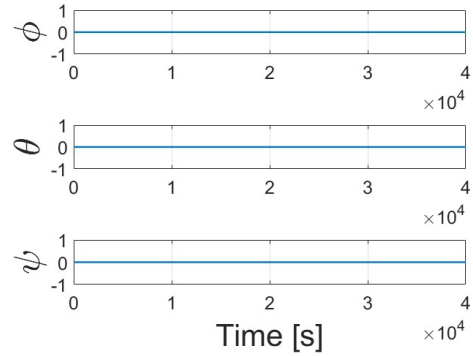


Figure 5.2: Euler Angles

observing its effect on the attitude. Under identical initial conditions but with a tumble rate of 20 degrees per second about the x axis, the attitude should exhibit a rotation about the x-axis (corresponding to the Euler angle ϕ), reaching 180 degrees in approximately 9 seconds. Thus, the initial velocity is set as $w_{oi} = \left[\frac{20\pi}{180}; -\sqrt{\mu/r^3}; 0 \right] \frac{rad}{s}$, ensuring the spacecraft starts in nadir configuration. The plot of the Euler angle ϕ is shown in Fig.5.3. This final verification can be performed for all three axes of the Body Reference

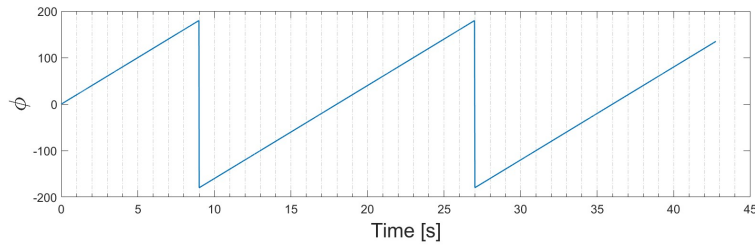


Figure 5.3: 20deg/s initial conditions

Frame and consistently yields expected results across each axis. These initial tests demonstrate that the spacecraft's attitude behaves as expected. Therefore, it can be considered successfully verified against the predicted behavior.

5.2 Gravity Gradient Verification

The validation of the gravity gradient disturbance has been conducted by implementing an alternative definition of the same torque and comparing it with the one derived from the existing definition used in our simulation, as referenced in Eq.4.5.

This alternative definition is described in [4], where the Gravity Gradient Torque is defined

as follows:

$$\begin{aligned}
 T_{ggx} &= \frac{3\mu}{2R_0^3}(I_z - I_y)\sin(2\phi)\cos^2(\theta) \\
 T_{ggy} &= \frac{3\mu}{2R_0^3}(I_z - I_x)\sin(2\theta)\cos(\phi) \\
 T_{ggz} &= \frac{3\mu}{2R_0^3}(I_x - I_y)\sin(2\theta)\sin(\phi)
 \end{aligned}
 \tag{5.1}$$

These equations have been implemented in the simulation, as illustrated in Fig.5.4. The resulting schemes have been compared with those previously obtained from the original simulation model to verify the validity of the modeling approach.

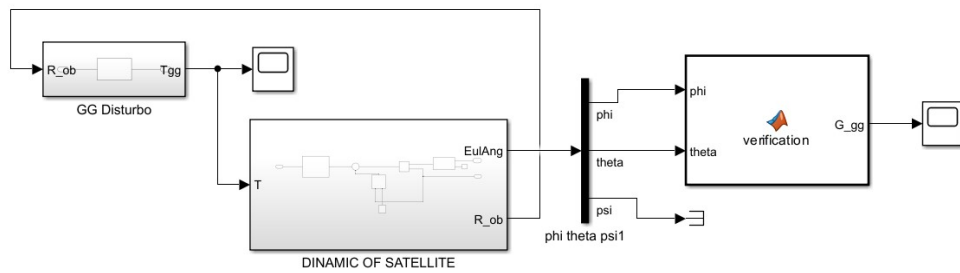


Figure 5.4: Gravity Gradient Implementation in MATLAB

To ensure the reliability of the simulation, both sets of functions were tested as inputs. The results, shown in Fig.5.5, indicate that the graphs produced by both implementations align perfectly, thereby confirming that the torque has been accurately validated and is reliable.

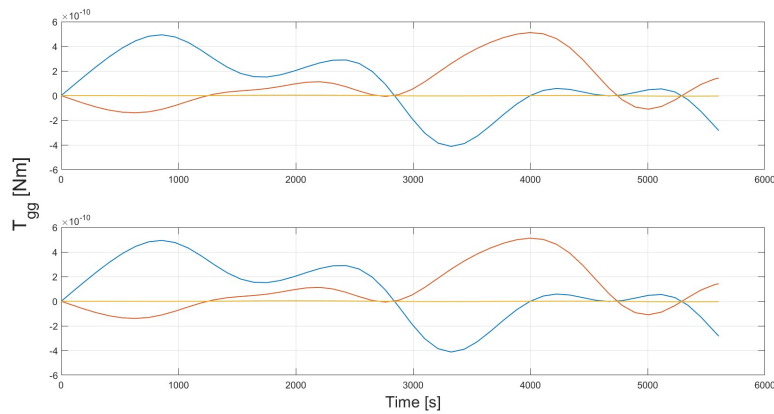


Figure 5.5: Gravity Gradient Torque in both implementations

In the upper part of the diagram, the simulation's Gravity Gradient Torque is shown, while the lower part displays the torque from the newly implemented model.

The z axis torque is zero, this can be explained when solely considering gravity gradient

torque. A PocketQube oriented with its z-axis towards nadir (Earth's center) and its x-axis in the orbital direction will experience non-zero torques only in the x and y axes. This arises because the gravity gradient torque acts to align the spacecraft's long axis with the direction of gravity. While the z-axis alignment minimizes the differential pull along that axis, the varying gravitational influence in the x and y directions creates torques that attempt to rotate the PocketQube, effectively inducing torques solely within the plane perpendicular to the nadir vector.

5.3 Aerodynamic Drag Verification

In order to verify the Aerodynamic Drag, it will be made a simulation with the type of Orbit 1 (refer to Section 3.1.3), and it will track the evolution of the Aerodynamic Drag Torque with time.

With the theoretical considerations done in Section 4.3, it can be predicted that if we simulate the propagation of the attitude of the PocketQube with only the Aerodynamic disturbances active, we'll expect to see the main component of the torque about the y-axis. In the body reference frame (see Section 2.2.1), the majority of the impacts of the molecules will be on the front face of the PocketQube, and so the torque will be on the y-axis. Additionally, a part of the torque will be about the z-axis because some molecules will also impact the sides of the PocketQube. Since the PocketQube has been modeled as a simple geometric shape, no torque will show about the x-axis.

The results of the simulation are shown below in Fig.5.6.

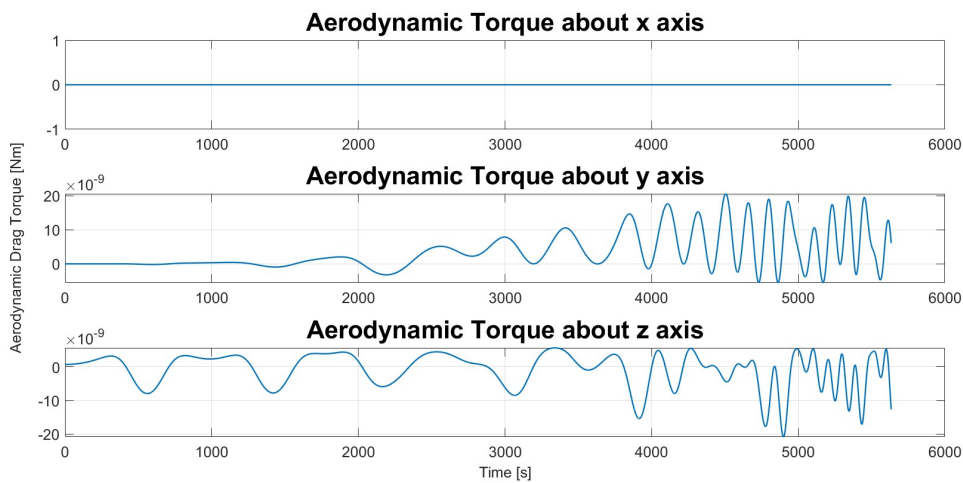


Figure 5.6: Aerodynamic Drag Torque

As can be seen, the torque meets the theoretical considerations discussed before and presents itself under the worst-case scenario predicted. Taking as input the data discussed in the previous chapter, we can obtain that the Aerodynamic Torque in the worst case is $T_{AD} = 3.21 \cdot 10^{-8}$.

Another consideration to be made is the fact that the angles are also representative of how a PocketQube under the influence of Aerodynamic Drag should behave. For example, in Fig.5.7, the angles between the velocity and the normal to the specific surface of the PocketQube are reported. The PocketQube has been divided into 6 faces. As we can see, the angle between the velocity and the z-axis begins as 90 degrees at the start of the simulation (which is valid because the start of the simulation is in nadir pointing mode) and decreases as the spacecraft is under the influence of the torque.

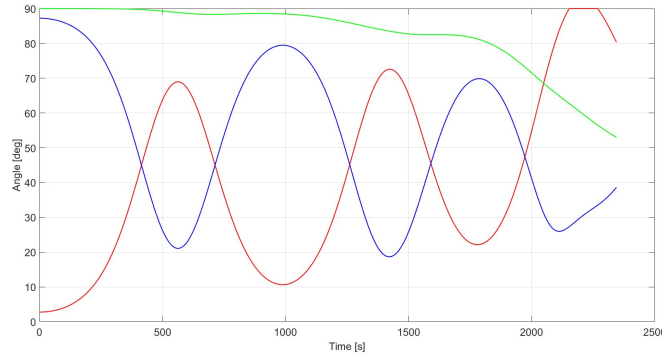


Figure 5.7: Angle between $\hat{\mathbf{N}}$ and $\hat{\mathbf{V}}$

In the figure, the red line represents the x-axis, the blue line represents the -y axis, and the green line represents the z-axis. All the angles refer to the body reference frame (see Section 2.2.1). Only some angles, such as those about the x, -y, and z axes, are represented. This is because it needs to be valid that $\hat{\mathbf{N}} \cdot \hat{\mathbf{V}} > 0$ (as discussed in Section 3.3), this means that the faces that are not exposed to the air flux are not experiencing the disturbances, as the theory says.

The consideration that this data brings us is that the torque implemented to model the Aerodynamic Drag is correct and can be considered valid for the purposes of the simulations.

5.4 Earth’s Magnetic Field Verification

Ensuring the accuracy of Earth’s magnetic field model is crucial for our spacecraft’s Attitude and Orientation Control System (AOCS), which relies heavily on precise magnetic field data. This verification confirms that the control torques accurately respond to the

relevant components of the magnetic field.

To validate this model, we utilized the built-in Simulink block designed to simulate the temporal progression of Earth's magnetic field¹. This block allows us to visualize the behavior of various magnetic field components over time. The results of this verification are illustrated in the figures below, which depict the x, y, and z components of the Earth's magnetic field. The simulation was conducted for Orbit Type 1 (refer to Section 3.1.3), with the start date set to January 1, 2025. The simulation extended over the duration of one complete orbit to capture a comprehensive view of the magnetic field's behavior. Below are the graphical results for each component.

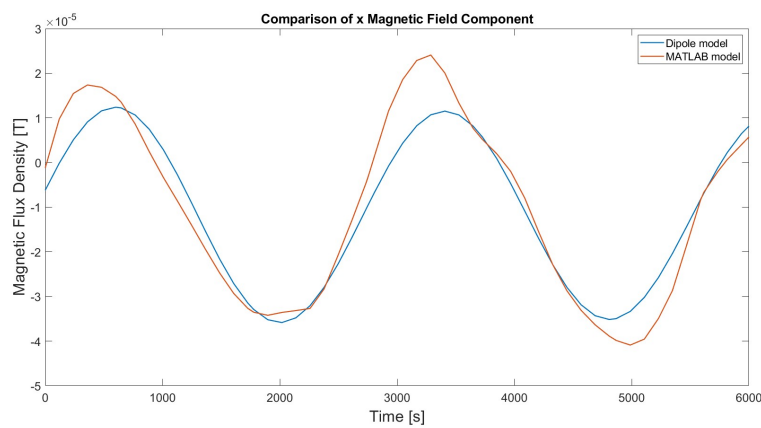


Figure 5.8: Comparison between the x Components

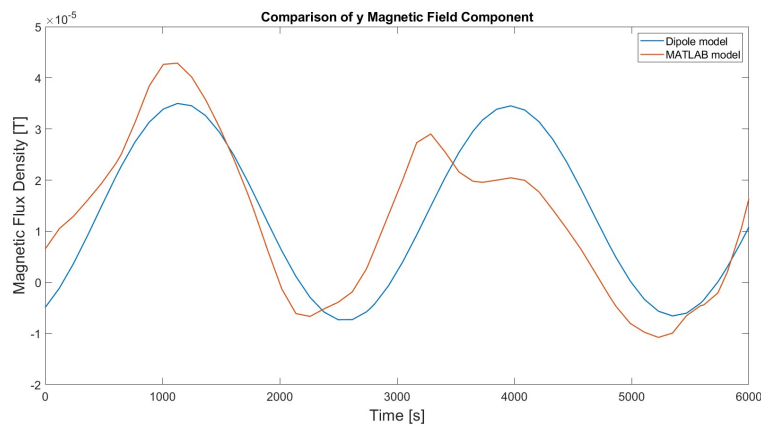


Figure 5.9: Comparison between the y Components

The figures show that while the simulated magnetic field is not perfectly accurate, but it serves as a reasonable first approximation for our purposes. The simulated field's progression appears more linear compared to the actual Earth's magnetic field, likely due to

¹<https://it.mathworks.com/help/aeroblks/internationalgeomagneticreferencefield.html>

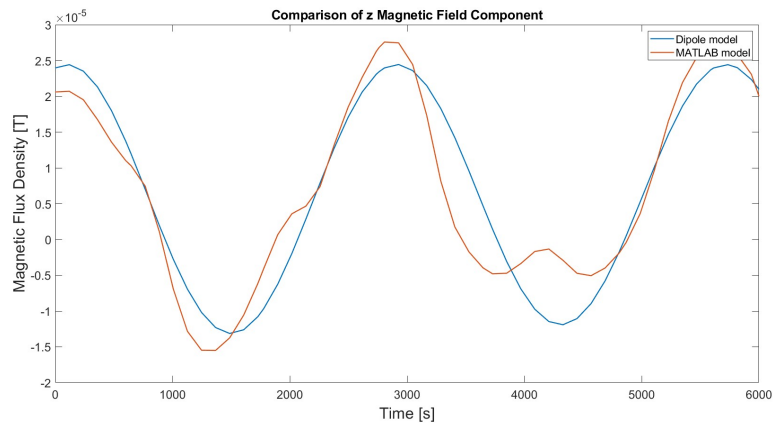


Figure 5.10: Comparison between the z Components

the model’s reliance on a dipole approximation expanded only to the first order (see Section 3.5.1). Despite this, the simulation captures the essential characteristics of Earth’s magnetic field, albeit with some limitations.

Additionally, an image of the error in Earth’s magnetic field approximation over time is provided. Since the error is minimal, we consider the model used in this simulation adequate.

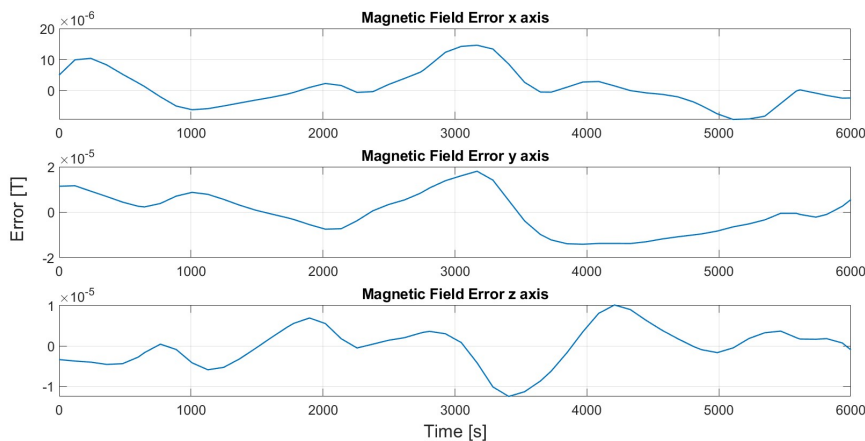


Figure 5.11: Errors Earth’s Magnetic Field

The MATLAB version of the magnetic field model can be employed for more accurate attitude simulations, though it demands significant computational power. This is because the Simulink block for the magnetic field provides data in North-East-Down (NED) coordinates. Converting these coordinates to Earth-Centered Inertial (ECI) or orbital coordinates requires substantial computational resources, resulting in longer simulation times. However, if necessary, the conversion to ECI coordinates has been implemented, complete with the necessary transformations, and is available for use.

Despite these limitations, the current model is sufficient for preliminary analysis and serves its intended purpose of providing a baseline environment for the AOCS. Future improvements could involve higher-order expansions of the magnetic field model, resulting in more detailed and accurate simulations. Such enhancements would enable a more precise representation of Earth’s magnetic field, ultimately improving the reliability and performance of the AOCS.

5.5 Permanent Magnet Torque

For the Permanent Magnet Torque, verification ensures that when only this torque is applied, it remains within the predicted minimum and maximum values, given that Earth’s Magnetic Field has already been verified and algebraic steps reviewed.

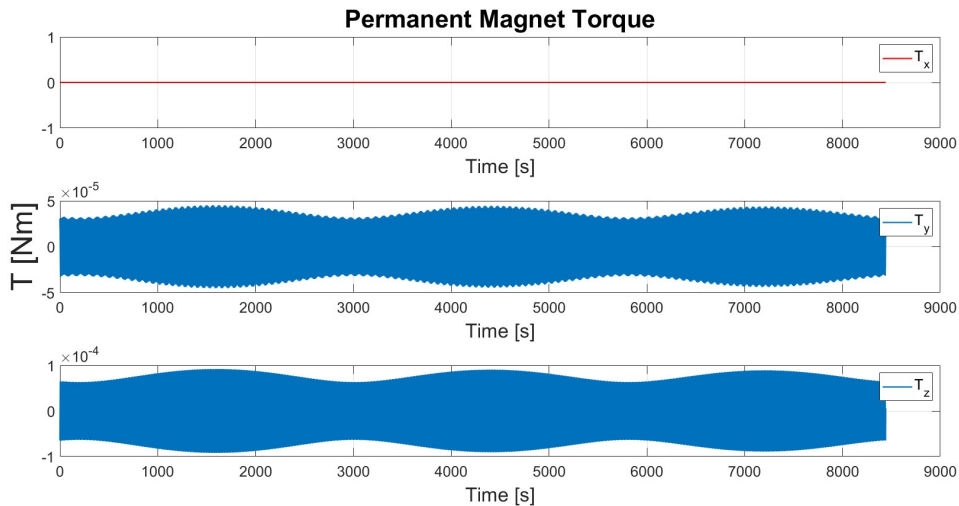


Figure 5.12: Permanent Magnet Torque Verification

The simulation was done for Orbit Type 1 (refer to Section 3.1.3). As shown, the torque stays between the predicted maximum value of $\pm 2.26910^{-4} Nm$ (given the maximum field value found in the IGRF model was 20,000 nT). The torque is not exerted about the x-axis, which is the axis of the dipole, and has maximum amplitude in the y-axis, predictable because the magnet behaves like a compass, and the field component is greater on the y-axis, resulting in greater torque.

5.6 Hysteresis Damping

To validate the accuracy of the hysteresis damping mechanism, the hysteresis cycles experienced by the material were compared against theoretical predictions. Data from the simulation were compared to expected theoretical outcomes.

The simulation conditions were set for Orbit Type 1 (see Section 3.1.3), with a propagation time of 11.11 hours, equivalent to approximately 7 orbits. This duration was chosen to evaluate the effectiveness of the damping action of the strips once initiated.

The simulation focused on observing the hysteresis cycles along the y_{BODY} and z_{BODY} axes, where the strips are strategically located. The resulting hysteresis cycles are illustrated in Fig.5.13 and Fig.5.14.

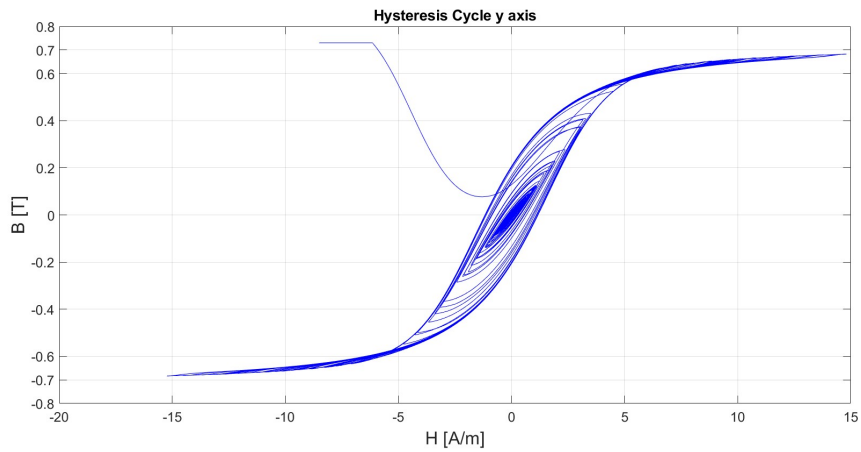


Figure 5.13: Hysteresis Cycle for y_{BODY} axis

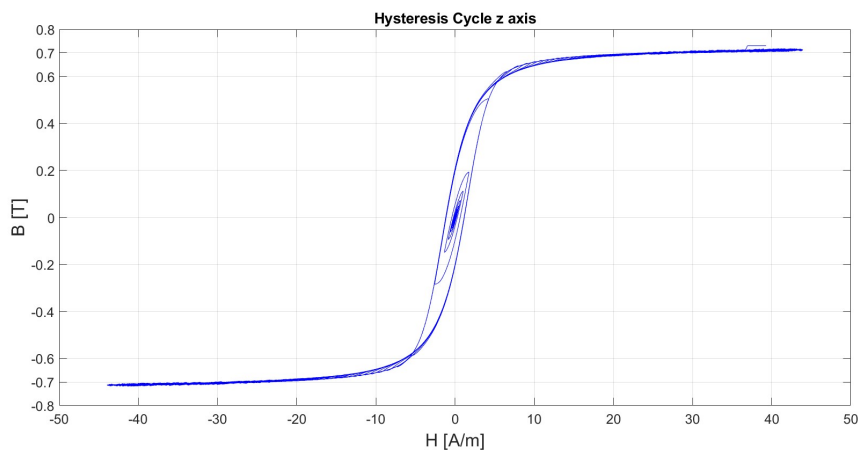


Figure 5.14: Hysteresis Cycle for z_{BODY} axis

The hysteresis cycles closely match theoretical expectations, demonstrating good accu-

racy in capturing the fundamental characteristics outlined in Section 3.5.3. Key features such as the induction saturation limit B_s , set at 0.73 T, are adhered to, as evidenced in Fig.5.15. This specific validation has been done for the z axis but is valid for the y axis as well. Deviations observed, such as those on the left in Fig.5.13, can be attributed to sim-

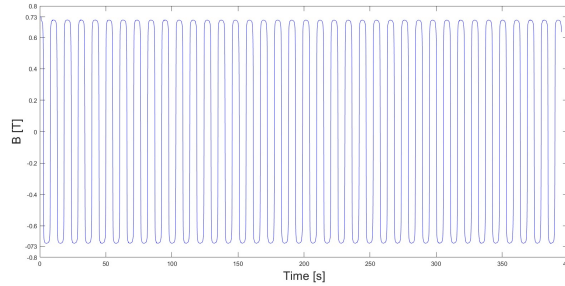


Figure 5.15: B_s limit

ulation accuracy limitations, which must be balanced to ensure efficient computational performance without compromising fidelity.

Another significant observation is the difference in area subtended by the graphs in Fig.5.14 and 5.13. This discrepancy aligns with expectations, as the strips along the z_{BODY} axis interact with a weaker component of the magnetic field compared to those along the y_{BODY} axis, and so will have to dampen less intense components of the field.

Another verification that can be done, is referring to a previous analysis and simulation of an hysteresis loop of a program that has already been verified such as SNAP ”Smart Nano-satellite Attitude Propagator” [22], here the same material is used and the result of the hysteresis loop is really close to the results obtained, this furthermore confirms that the model is valid. It is shown in Fig.5.16.

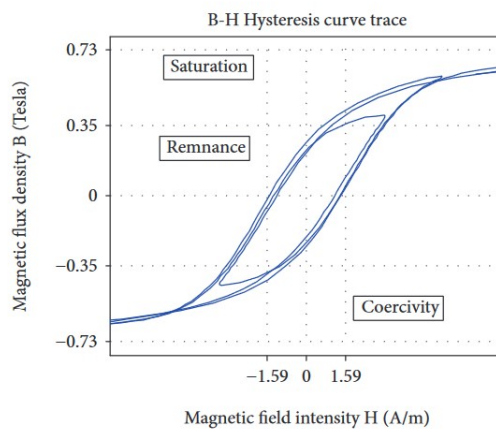


Figure 5.16: SNAP hysteresis loop [24]

In conclusion, the simulation validates that the hysteresis damping mechanism operates effectively, accurately reflecting theoretical concepts and meeting practical design requirements for the spacecraft's attitude control system.

Accurate simulation and validation of hysteresis cycles play a pivotal role in enhancing the spacecraft's attitude control system. Hysteresis damping strips counteract unwanted oscillations that can destabilize the spacecraft's orientation during maneuvers. Through rigorous simulation and validation, hysteresis damping strips ensure the spacecraft's attitude control system operates effectively.

5.7 Monte Carlo simulation

Monte Carlo simulation is a statistical technique used to model and analyze complex systems that involve uncertainty and variability. It relies on random sampling and statistical analysis to obtain numerical results. By simulating a process thousands of times, Monte Carlo methods provide a probability distribution of possible outcomes, allowing for the estimation of risk and uncertainty in decision-making.

Monte Carlo simulation is essential for testing the robustness of a program because it helps identify how the program behaves under a wide range of conditions. This is crucial in verifying the program's reliability, especially when dealing with uncertain inputs or complex systems where analytical solutions are impractical. By repeatedly running the program with varied inputs, one can observe its performance, detect potential flaws, and ensure that it consistently produces accurate results. This robustness testing is vital for programs used in critical applications, such as engineering design, and scientific research, where failure or inaccuracies can have significant consequences.

In the context of the ADCS simulation, Monte Carlo simulation is useful to identify how the ADCS behaves when dealing with random inputs, such as those it will receive in real-life conditions.

Due to time constraints, the Monte Carlo simulation run for this program is relatively small but provides a preliminary look into the program's robustness.

Two main variables were varied in an uniform range:

- Initial Angular Rate ω_{BI0} : It was varied in a range of $\pm 20\%$ from the initial value of 10 deg/s, divided in 5 values.
- Permanent Magnet flux density B_r : it was chosen to be in a range of $1.32 \div 1.38$, the values displayed in the magnet datasheet, this range was divided in 4 values.

This results in a total of 20 combinations. While this Monte Carlo simulation is not exten-

sive, it serves as a first approximation for testing the simulation's reliability and robustness, and to see how the program behaves with a changing range of values.

The outputs to be analyzed are the mean of the angular rates and the angle between the permanent magnet and the Earth's magnetic field.

As illustrated in Fig.5.17, the mean behaviour of the angular rate ω_x aligns well with theoretical expectations and simulation results. Although some oscillations in the angular rate appear amplified, the overall behavior accurately represents the angular rate. When interpreting the simulation outcomes, it's crucial to consider these results critically.

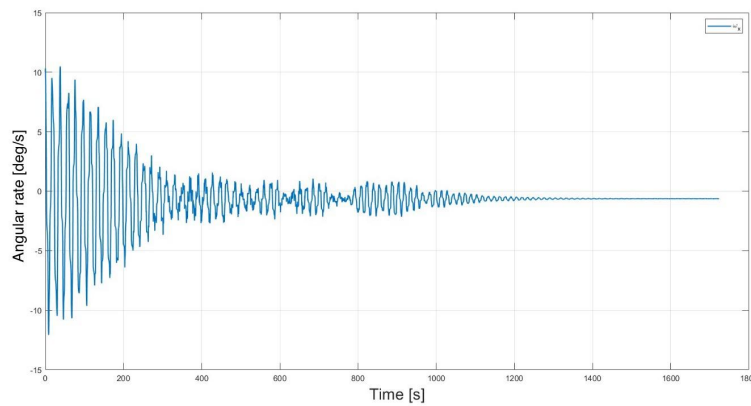


Figure 5.17: Mean ω_x angular rate

The result of the ω_y component is shown in Fig.5.18. As expected the mean angular rate converge to zero, indicating that the simulation of this component is robust and correct.

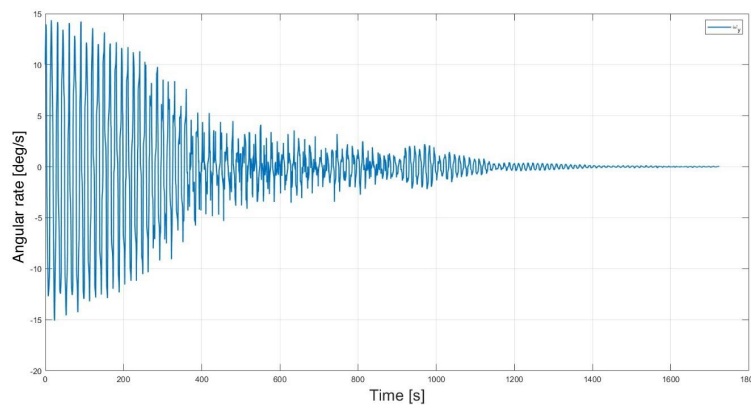


Figure 5.18: Mean ω_y angular rate

Finally all the mean angular rate components are displayed in Fig.5.19, as can be seen the only angular rate that is not compliant with what was predicted is the ω_z component. The

component should have converged to zero, this indicates that the simulation results must be interpreted with some discrepancies from real-life conditions.

The confidence intervals are also being calculated, they are ranges within which a pop-

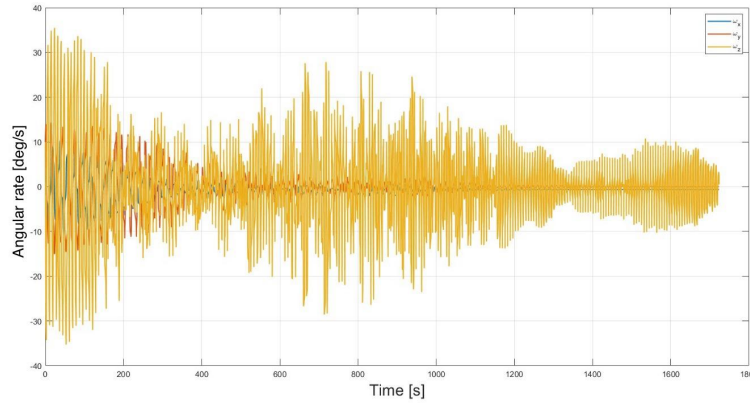


Figure 5.19: Mean angular rates

ulation parameter, such as a mean or proportion, is expected to lie with a certain level of confidence. They provide an estimate of the uncertainty associated with a sample statistic, indicating how much variability is expected if the study were repeated multiple times. For this case study the confidence intervals are set at 95%. The initial and final values for the angular rates of all components are shown in Tab.5.1.

The confidence intervals indicate that the program behaves as predicted by theory, demon-

	Confidence Interval	
	Initial value [deg/s]	Final value [deg/s]
CI ω_x	10.64 ÷ 9.36	-0.58 ÷ -0.68
CI ω_y	10.64 ÷ 9.36	0.046 ÷ -0.023
CI ω_z	10.64 ÷ 9.36	5.95 ÷ -3.51

Table 5.1: Angular Rates Confidence Intervals

strating robustness and goal compliance.

This behavior can also be observed from the angle between the Earth's magnetic field and the permanent magnet's orientation. Fig.5.20 shows that the permanent magnet converges and starts to track the magnetic field, but with a certain misalignment. This is due to the same reason discussed earlier. The simulation results must be evaluated with the understanding that real-life conditions will introduce uncertainties due to this factor.

Confidence intervals are also provided for this value type and are reported in Tab5.2. These intervals help quantify the uncertainty associated with the simulation results, reflecting the variability that could occur if the experiment were repeated multiple times

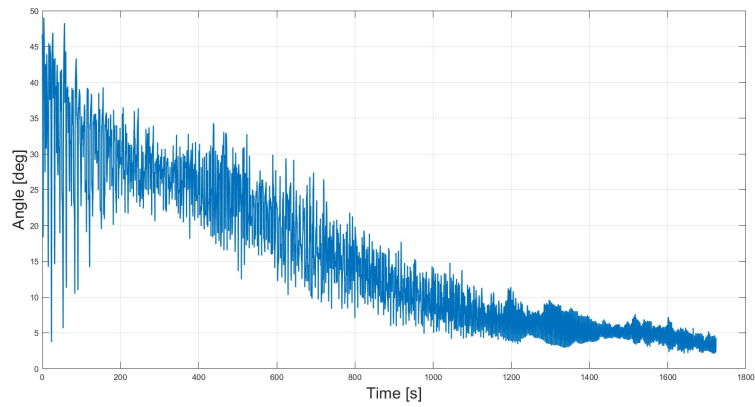


Figure 5.20: Mean Angle

	Confidence Interval	
	Initial value [deg]	Final value [deg]
CI	46.18 ÷ 46.18	4.25 ÷ 1.82

Table 5.2: Angle Confidence Intervals

under similar conditions.

As can be seen from these evaluations the simulation shows a good robustness and behaves very well to changing ranges, as can be the ones of a real-life situation.

Chapter 6

Simulation Results and Analysis

This chapter is dedicated to presenting and analyzing the results obtained from the simulation of the passive attitude control system for the PocketQube of the J2050 mission. It will be examined the behavior of the spacecraft under the influence of all acting torques, providing a comprehensive analysis of these results in the context of the current mission. Furthermore, the outcomes will be compared with those from previous missions to evaluate the effectiveness and reliability of the passive control strategy. This comparative analysis aims to highlight the improvements and potential areas for future enhancement in the design and implementation of passive attitude control systems for small satellites like PocketQube.

The simulations were conducted using the input parameters specified in Chapter 3 and tested with two different types of orbits, as detailed in Section 3.1.3.

For each orbit, the following results were analyzed:

- Angular Velocity in the Body Reference Frame ($\omega_x, \omega_y, \omega_z$): This analysis helps determine the time required for the system to dampen and the final angular rate once the system stabilizes.
- Euler Angles Relative to the Body Reference Frame (ϕ, θ, ψ): Observing these angles allows to understand the satellite's attitude behavior over time.
- Angle Between the Permanent Magnet and the Earth's Magnetic Field: This metric is used to assess when the magnet begins to track the Earth's magnetic field and the accuracy of this alignment.

To simplify and help to understand these results it is provided an image of the Body Reference Frame on the PocketQube (for further details refer to Section 2.2.1), Fig.6.1 represents how the Body Reference System is set and the reader is reminded that the permanent

magnet is placed with its dipole directed along the x axis and the hysteresis strips along the y and z axis.

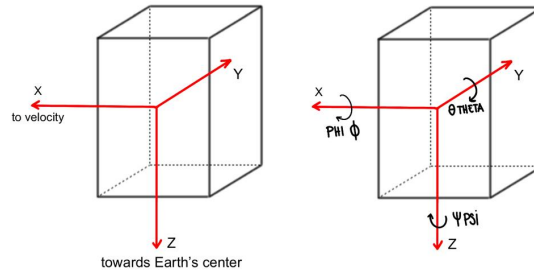


Figure 6.1: Body Reference Frame and Euler Angles

Additionally, these results were obtained by imposing an angular rate on all axis of 10 deg/s. These results are crucial for understanding the system's performance and stability in orbit.

6.1 Orbit 1 Results

The simulation conducted for Orbit 1 was for a total of 8 orbits, in order for the PocketQube to dampen and stabilize over time.

Fig.6.2 shows the result of the angular rates for the three axis. The system can be considered completely damped in about 45 minutes, only a residual angular rate is left on the x axis. This behaviour is predictable from theoretical considerations because the dipole is oriented along the x axis itself, consequently being uncontrollable. As can be seen from Fig.6.3, that shows the Euler Angles, the attitude of the angle around the x axis "φ" is uncontrolled and will roll about the x axis 11 times per orbit.

The other Euler angles show more controlled variations. The angle about the y axis, θ , fluctuates between ± 60 deg, this value may represent a problem since it affects the telecommunication system, it needs to be reconsidered in order to evaluate the severity of the issue. The angle about the z axis "ψ" varies between $-45 \div -130$ deg, behaving as a compass needle, this angle doesn't influence the overall "nadir pointing" orientation of

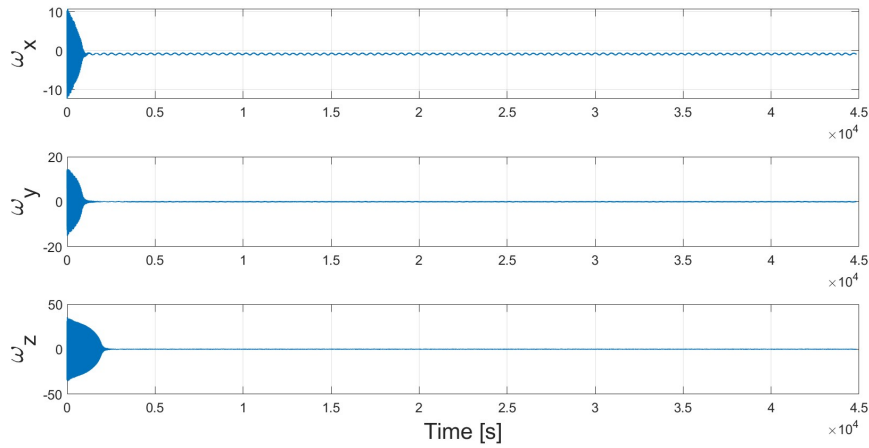


Figure 6.2: Angular Rates in Body Reference Frame Orbit 1

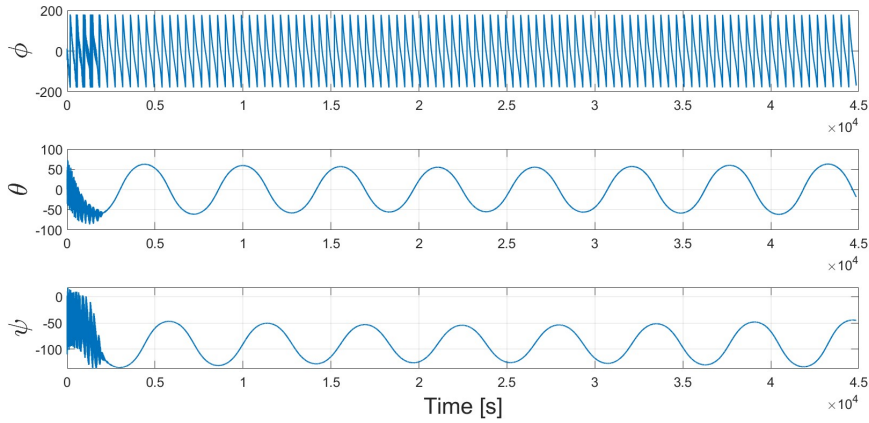


Figure 6.3: Euler Angles Orbit 1

the spacecraft, so it can be considered acceptable.

Fig.6.4 shows that the permanent magnet starts to track the Earth's magnetic field in about 48 minutes from orbit insertion.

After 45 minutes the angular rates stabilize as follows:

- $\omega_x = -0.5 \div -1 \text{ deg/s}$
- $\omega_y = 0 \text{ deg/s}$
- $\omega_z = 0 \text{ deg/s}$

Although the rotation affects the spacecraft's nadir-pointing configuration, it still provides sufficient windows for taking Earth photos and testing devices (CRYSTAL). Thus, 11 rotations per orbit are acceptable.

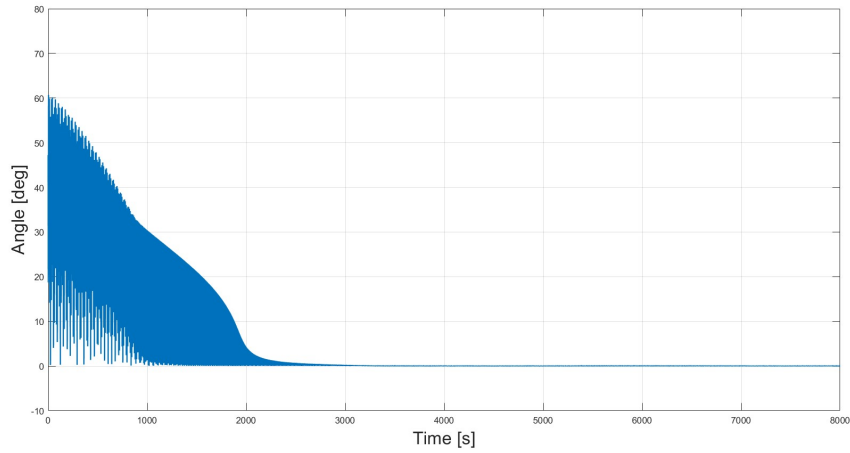


Figure 6.4: Permanent Magnet/Earth's Magnetic Field Angle Orbit 1

6.2 Orbit 2 Results

Orbit Type 2 has an inclination of 98 degrees, this comes as unfavorable for this type of attitude control, due to the more inclined magnetic field and close passes to the Earth's magnetic poles. Fig.6.5 shows the angular rates relative to all three axes.

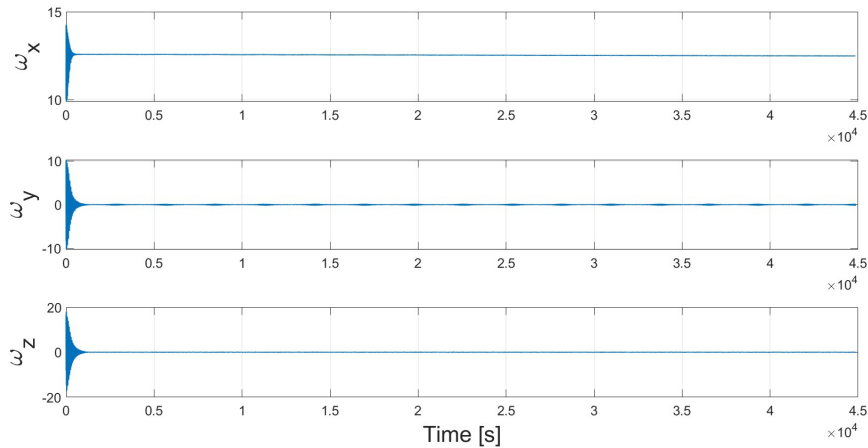


Figure 6.5: Angular Rates in Body Reference Frame Orbit 2

The system dampens in 27 minutes from orbit insertion. However w_y will show small increases of the angular rate when the spacecraft passes through the poles of the magnetic field. w_x stabilizes at 12.5 degrees per second, displaying a pattern of decreasing angular rate over time.

Fig.6.6 shows the Euler Angles, as can be seen from the figure, the angle about the axis of the permanent magnet " ϕ " is greatly affected by the variation of the inclination of the

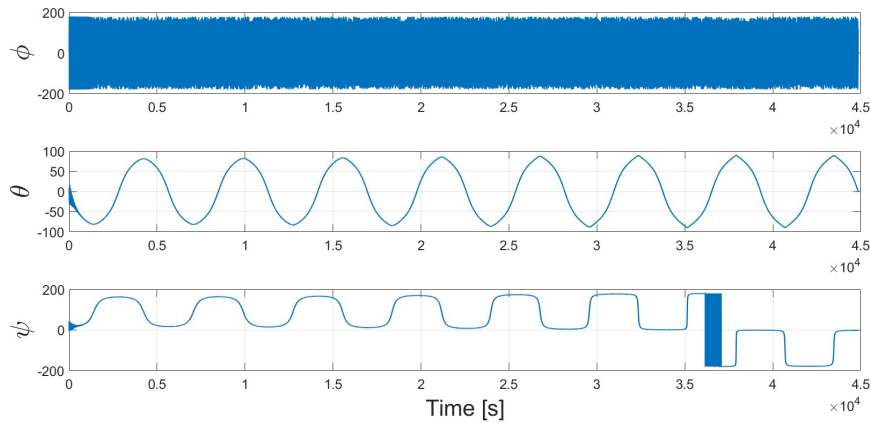


Figure 6.6: Euler Angles in Body Reference Frame Orbit 2

orbit. As can be seen from a zoom in Fig.6.7, it will rotate 190 times per orbit. This value needs to be evaluated carefully to see if it is acceptable for the camera subsystem.

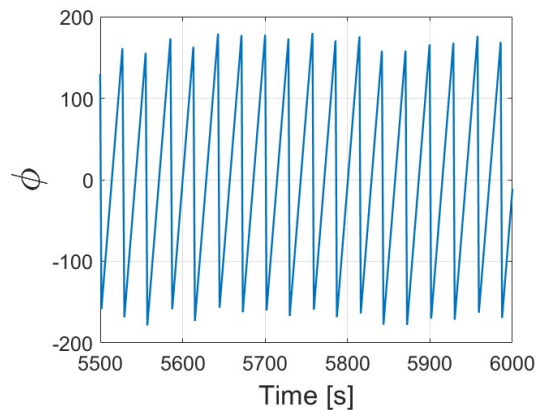


Figure 6.7: Zoom of Euler Angles

It can also be noticed that there is a pattern of inversion every 10 hours of the ψ angle, potentially causing issues for the debris impact sensor.

Lastly, we can analyze the tracking of the Earth's magnetic field, as can be seen from Fig.6.8, the tracking begins after 17 minutes from orbit insertion.

In conclusion, in this configuration the system will dampen quicker but the attitude reveals as more chaotic.

The choice of attitude control strategy should consider the trade-offs of each scenario.

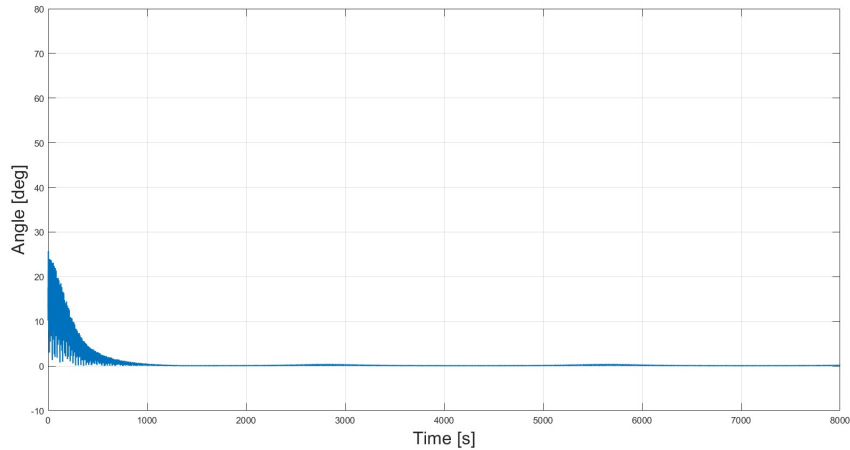


Figure 6.8: Permanent Magnet/Earth's Magnetic Field Angle Orbit 2

6.3 Summary and Comparative Analysis of ADCS Results

Based on the results already displayed, the choice of the Orbit Type 1 proves to be favourable, despite requiring a longer time to dampen the system. This orbit type results in more controlled spacecraft attitude.

The challenges encountered applied to the J2050 mission, are primarily focused on two main aspects:

- Antenna Communication Angle θ (about the y axis): For effective communication, the antenna must remain within the range of $-50 \div +50$ degrees, currently it exceeds this range by 10 degrees. It is crucial to determine if the intervals during which the antenna won't be able to communicate are acceptable or if alternative solutions are required.
- Impact Sensor Positioning ψ (about the z axis): The impact sensor needs to measure debris by aligning with the velocity direction. Variations of the angle means could result in the sensor failing to track debris impacts consistently. Choosing Orbit Type 2 might exacerbate this issue due to its pattern of inversion.

The selected Attitude Determination and Control System (ADCS) demonstrates high efficiency compared to other existing systems. However, this comparison primarily uses data from CubeSats, and the size difference must be considered. CubeSats are generally more resistant to external torques but respond slower to control torques, such as those from a permanent magnet or a soft ferromagnetic material. This affects the damping time and the

velocity needed to track Earth's magnetic field.

A relevant case study involves the 1U CubeSat "Quetzal-1" [25], which operated from April to November 2020. The ADCS of Quetzal-1 was examined, showing that the CubeSat has a permanent magnet with lower magnetic flux density and uses two larger hysteresis strips of the same material. It is to be considered that Quetzal-1 is also twice the size of the PocketQube. The reported rotational rates post-deployment were between $-25 \div +25$ deg/s, so another simulation was run in order to compare the results with the model used in J2050. The angular velocity of the axis of the permanent magnet in Quetzal-1 stabilized at 2.8 deg/s, increasing pattern to 3.5 deg/s over time. The J2050 system dampened within one orbit for the simulation, whereas Quetzal-1 took three days, attributable to the stronger magnet and smaller size of the PocketQube.

The simulation predicts that the PocketQube's rotational rate will stabilize at approximately -2 deg/s, which is smaller compared to the one of Quetzal-1. The larger angular rate of Quetzal-1 suggests potential unexpected environmental disturbances. Notably, the article mentions an increase in the angular rate of Quetzal-1's magnet axis after a month in orbit, indicating another area for further investigation.

While the PocketQube's simulation offers a solid initial approximation of the ADCS behavior in orbit, further adjustments and considerations based on previous spacecraft experiences are necessary. Overall, the selected passive ADCS is efficient for the mission's goals and provides adequate control for the PocketQube. However, the critical issues identified need careful evaluation to determine their impact on mission success.

Chapter 7

Conclusions

The simulator described in this thesis aims to model the attitude propagation of the J2050 mission PocketQube, which is controlled by a passive magnetic ADCS system.

This system can be varied to test different configurations. Major environmental disturbances were implemented in Simulink, along with the control torques and the hysteresis cycle for angular rate damping.

The system takes as input the design and initial mission values of the satellite and the values of the architecture of the passive control system, it reads them and propagates the satellite's attitude and perturbations throughout the orbit. At each time step, the torques are calculated based on the Earth's magnetic field at that point, the spacecraft's velocity, and the satellite's orientation.

Passive magnetic control systems are ideal for missions that do not have stringent pointing accuracy requirements. The strength of the permanent magnets depends on the orbit's altitude, the Earth Magnetic Field intensity and the environmental torques experienced. A simulation tool that can demonstrate the dynamic response of the system is a valuable device for experimenting with different configurations and architectures of the ADCS system.

The environmental model designed in this simulator can also serve as a foundation for future work, including the simulation of active ADCS systems or hybrid ones.

As demonstrated in the final chapter of this thesis, the solution adopted for the J2050 mission appears consistent and provides the necessary pointing accuracy to achieve the mission's objectives, with the added advantage of not requiring any moving parts or power consumption.

The successful implementation and validation of this simulator highlight its potential as a versatile tool for ADCS design and testing of PocketQube missions. This tool's ability to simulate the dynamic response of different ADCS configurations makes it an invaluable

resource for the development of small satellite missions, providing insights into system performance and aiding in the optimization of control strategies.

7.1 Limitations and Future Work

Probably the main challenge encountered in building the simulator was defining the Earth's magnetic field, which is crucial for the type of control required. Future work should focus on expanding the harmonic function in order to develop a more representative version of the magnetic field. This will ensure the most reliable magnetic field possible, thereby improving the accuracy of the control system representation.

Another important area for future work should also focus on testing the hysteresis cycle of soft ferromagnetic materials in laboratory. To verify the behavior of the material under real-life conditions, laboratory tests are essential. These tests will assess the performance of the material and, if necessary, adjustments can be made to the simulator to enhance its accuracy.

Furthermore, the shape of the PocketQube must be detailed further. Shifting the center of mass from the geometric center will provide a more realistic representation of the satellite's mass distribution. The best estimation of the inertia characteristics of the PocketQube will be obtained when the spacecraft is built and can be measured directly.

To enhance the accuracy of the representation of the environment, a model for the SRP (Solar Radiation Pressure) torque should also be built. Including this model will create a more reliable simulation scenario.

Future work will include a more detailed and extensive Monte Carlo simulation. Conducting a larger number of simulations will allow for a more effective assessment of the program's reliability.

Additionally, exploring an active ADCS control scheme should be considered. This approach will address the limitations encountered when adapting the passive control system to the mission goals. An active control system would improve the ability to maintain the required antenna angle for communication and provide better overall attitude control for the spacecraft.

These improvements will pave the way for more sophisticated and effective ADCS representation and strategy for the J2050 mission in the future.

Bibliography

- [1] F.Toson. *Fly Your Satellite! 4 "RedPill"*. ESA, 2024. isbn: 9780201157901.
- [2] Radu S. et al. "The PocketQube Standard". In: (2018).
- [3] Radu S. et al. "Utility and constraints of PocketQubes". In: *CEAS Space Journal* (2020).
- [4] Sidi M.J. *Spacecraft Dynamics and Control*. Cambridge University Press, 1997. isbn: 9780201157901.
- [5] Damaren C. De Ruiter A. and Forbes J. *Spacecraft Dynamics and Control: An introduction*. Wiley, 2013.
- [6] Karpenko S.O. "Attitude Control System of the First Russian Nanosatellite TNS-0 no. 1". In: *Kosmicheskie Issledovaniya* (2010).
- [7] Ovchinnikov M. "Attitude dynamics of the first Russian nanosatellite TNS-0". In: *Acta Astronautica* (2007).
- [8] Santoni F. et al. "Soft Magnets for Passive Attitude Stabilization of Small Satellites". In: *IEEE Transaction on Magnetics* (2010).
- [9] Ousaloo H. S. "Hysteresis Nutation Damper for Spin Satellite". In: *The Open Aerospace Engineering Journal* (2013).
- [10] Curtis H. *Orbital Mechanics for Engineering Students*. Embry-Riddle Aeronautical University, Daytona Beach, Florida, 2005.
- [11] Campbell P. *Permanent Magnet Materials and their Application*. Cambridge University Press, 1994.
- [12] Coey J. *Rare-Earth Iron Permanent Magnets*. Oxford University Press, 2012.
- [13] Croat J.J. and Snyder J.E. *Modern Permanent Magnets*. Cambridge University Press, 2021.
- [14] Panda A.K. "Microstructure and Magnetic Properties of NdFeB Magnets". In: *Science and Engineering: B*, 176(20), 1444-1450. DOI: 10.1016/j.mseb.2011.09.022 (2011).

- [15] Brown D. “A Review on the Enhancement of NdFeB Permanent Magnet Performance”. In: *Journal of Magnetism and Magnetic Materials* (2002).
- [16] Spaldin N.A. *Magnetic Materials: Fundamentals and Applications*. Cambridge University Press, 2010.
- [17] Wertz J.R. *Spacecraft Attitude Determination and Control*. Kluwer Academic Publishers, 1990.
- [18] Fernández J. “Design of a PocketQube Passive Attitude Control System”. In: *Fossa Systems* (2019).
- [19] John L. Crassidis F. Landis Markley. *Fundamentals of Spacecraft Attitude Determination and Control*. Springer, 2014.
- [20] Shigemoto F.H. White J.S. and Bourquin K. “Satellite Attitude Control Utilizing the Earth’s Magnetic Field”. In: *NASA Technical Note* (1961).
- [21] International Association of Geomagnetism and Aeronomy (IAGA). December 2019. url: <https://www.ncei.noaa.gov/products/international-geomagnetic-reference-field>.
- [22] Rawashdeh S.A. “PASSIVE ATTITUDE STABILIZATION FOR SMALL SATELLITES”. MA thesis. University of Kentucky, 2010.
- [23] Henrett D.A. Flatley T.W. “A MAGNETIC HYSTERESIS MODEL”. In: *NASA/GSFC Code 712* ().
- [24] Rawashdeh S.A. “Attitude Analysis of Small Satellites Using Model-Based Simulation”. In: *Electrical and Computer Engineering, University of Michigan-Dearborn, Dearborn, MI 48128, USA* (2019).
- [25] Alvarez D. et al. “Design and On-Orbit Performance of the Attitude Determination and Passive Control System for the Quetzal-1 CubeSat”. In: *A. Deepak Publishing* (2023).